

DEVELOPMENT AND APPLICATION OF NOVEL METAL OXIDE FOR  
HIGH-EFFICIENCY SILICON SOLAR CELLS

A THESIS SUBMITTED TO  
THE GRADUATE SCHOOL OF NATURAL AND APPLIED SCIENCES  
OF  
MIDDLE EAST TECHNICAL UNIVERSITY

BY

GÖKHAN ALTINER

IN PARTIAL FULFILLMENT OF THE REQUIREMENTS  
FOR  
THE DEGREE OF MASTER OF SCIENCE  
IN  
MICRO AND NANOTECHNOLOGY

AUGUST 2025



Approval of the thesis:

**DEVELOPMENT AND APPLICATION OF NOVEL METAL OXIDE FOR  
HIGH-EFFICIENCY SILICON SOLAR CELLS**

submitted by **GÖKHAN ALTINER** in partial fulfillment of the requirements for  
the degree of **Master of Science in Micro and Nanotechnology, Middle East  
Technical University** by,

Prof. Dr. Naci Emre Altun  
Dean, **Graduate School of Natural and Applied Sciences** \_\_\_\_\_

Prof. Dr. Hüsni Emrah Ünalın  
Head of the Department, **Micro and Nanotechnology** \_\_\_\_\_

Prof. Dr. Raşit Turan  
Supervisor, **Micro and Nanotechnology, METU** \_\_\_\_\_

Dr. Hisham Nasser  
Co-Supervisor, **Micro and Nanotechnology, METU** \_\_\_\_\_

**Examining Committee Members:**

Prof. Dr. Emrah Görkem Günbaş  
Chemistry, METU \_\_\_\_\_

Prof. Dr. Raşit Turan  
Physics, METU \_\_\_\_\_

Assoc. Prof. Dr. Selçuk Yerci  
Electrical – Electronics Engineering, METU \_\_\_\_\_

Assoc. Prof. Dr. Mustafa Kulakçı  
Physics, Eskişehir Technical Uni. \_\_\_\_\_

Prof. Dr. Serap Güneş  
Physics, Yıldız Technical Uni. \_\_\_\_\_

Date: 26.08.2025

**I hereby declare that all information in this document has been obtained and presented in accordance with academic rules and ethical conduct. I also declare that, as required by these rules and conduct, I have fully cited and referenced all material and results that are not original to this work.**

Name Last name : Gökhan Altıner

Signature :

## ABSTRACT

### DEVELOPMENT AND APPLICATION OF NOVEL METAL OXIDE FOR HIGH-EFFICIENCY SILICON SOLAR CELLS

Altiner, Gökhan  
Master of Science, Micro and Nanotechnology  
Supervisor: Prof. Dr. Raşit Turan  
Co-Supervisor: Dr. Hisham Nasser

August 2025, 72 pages

This thesis investigates the development and application of two novel metal oxide-based passivating contacts designed to minimize carrier recombination and resistive losses in high-efficiency silicon solar cells. Hydrogenated Aluminum-doped Zinc Oxide (AZO:H) was developed via spatial atomic layer deposition (ALD) as a transparent, electron-selective contact for Tunnel Oxide Passivated Contact (TOPCon) solar cells. Molybdenum Oxide ( $\text{MoO}_x$ ) was developed via thermal evaporation as a hole-selective contact for Passivated Emitter and Rear Contact (PERC) solar cells. The passivation quality of an optimized AZO:H/ $\text{AlO}_x$  stack on n-type poly-Si was exceptional, yielding an  $iV_{oc}$  of 728 mV and a  $J_0$  of 7.5 fA/cm<sup>2</sup> after a commercially viable  $\text{N}_2$  anneal. Concurrently, the successful integration of  $\text{MoO}_x$  into an industrial PERC process flow was demonstrated. A champion power conversion efficiency of 21.53% was realized for a large-area industrial Cz p-type cell featuring an optimized 5 nm local  $\text{MoO}_x/\text{Ag}$  back contact. This performance was driven by a high fill factor of 80.66% and a  $V_{oc}$  of 672.3 mV, validating the contact's

effectiveness. These findings demonstrate the high potential of both AZO:H and MoO<sub>x</sub> as effective, low-temperature processed passivating contacts, offering distinct and promising pathways to enhance the performance of next-generation crystalline silicon solar cell architectures.

Keywords: Passivating Contacts, Photovoltaics, Transparent Conductive Oxides, Solar Cells.

## ÖZ

### YÜKSEK VERİMLİ SİLİSYUM GÜNEŞ HÜCRELERİ İÇİN METAL OKSİTLERİN GELİŞTİRİLMESİ VE UYGULANMASI

Altınır, Gökhan  
Yüksek Lisans, Mikro ve Nanoteknoloji  
Tez Yöneticisi: Prof. Dr. Raşit Turan  
Ortak Tez Yöneticisi: Dr. Hisham Nasser

Ağustos 2025, 72 sayfa

Bu tez, yüksek verimli silisyum güneş hücrelerinde yük rekombinasyonu ve direnç kayıplarını en aza indirmek için tasarlanmış iki metal oksit tabanlı pasifleştirici kontakın geliştirilmesini ve uygulanmasını araştırmaktadır. Hidrojenlendirilmiş Alüminyum katkılı Çinko Oksit (AZO:H), TOPCon güneş hücreleri için şeffaf, elektron seçici bir kontak olarak atomik katman biriktirme (ALD) yoluyla geliştirilmiştir. Molibden Oksit ( $\text{MoO}_x$ ), PERC güneş hücreleri için pozitif yük seçici lokal kontak olarak termal buharlaştırma yoluyla geliştirilmiştir. n-tipi poli-Si üzerinde optimize edilmiş AZO:H/ $\text{AlO}_x$  filmlerin pasivasyon kalitesi oldukça yüksek olup, ticari olarak uygulanabilir  $\text{N}_2$  tavlamasından sonra 728 mV'luk bir  $iV_{oc}$  ve 7.5 fA/cm<sup>2</sup>'lik bir  $J_0$  değeri vermiştir. Buna ek olarak,  $\text{MoO}_x$ 'in endüstriyel bir PERC üretim akışına başarılı entegrasyonu gösterilmiştir. Optimize edilmiş 5 nm'lik yerel bir  $\text{MoO}_x/\text{Ag}$  arka kontakına sahip büyük alanlı endüstriyel Cz p-tipi hücre için %21.53'lük rekor bir verimlilik elde edilmiştir. Bu performans, %80.66'lık yüksek bir FF ve 672.3 mV'luk bir  $V_{oc}$  değeri ile sağlanmış olup, kontakın etkinliğini doğrulamıştır. Bu bulgular, hem AZO:H'nin hem de  $\text{MoO}_x$ 'in, yeni nesil kristal

silisyum güneş hücresi dizaynlarının performansını artırmak için farklı ve umut vadeden yollar sunan, etkili, düşük sıcaklıkta işlenmiş pasifleştirici kontaklar olarak yüksek potansiyelini göstermektedir.

Anahtar Kelimeler: Kontak Pasivasyonu, Fotovoltaik, Saydam İletken Oksitler, Güneş Hücreleri.

To my family and friends

## ACKNOWLEDGMENTS

First and foremost, I would like to express my sincere thanks to my advisor, Prof. Dr. Raşit Turan, for his constant support and encouragement throughout my master's journey, and I am deeply grateful for his mentorship. I also owe a great debt of thanks to my co-advisor, Dr. Hisham Nasser. His patience and invaluable help were essential to the completion of this thesis, and I am truly thankful for his guidance every step of the way.

I owe a special thanks to my lab mates and friends, Yiğit Mert Kaplan, Eni Muka, and Berkay Uygun. I am so grateful for the time we spent together, from sharing meals and coffee to taking classes and working late hours. Their friendship, support, and assistance with my thesis were a constant source of motivation. Their presence not only enriched my academic life but also made this entire experience a truly memorable one.

I would like to sincerely thank the ODTÜ-GÜNAM team. Special thanks to İlkcan Erdem, Seda Kılıçkaya, Meryem Ezgi Kına, Batuhan Taş, Cem Maden, Dr. Ayşe Can, Dr. Milad Gasemi, Arghavan Salimi, Mustafa Büyükgüzel, İrem Nur Manaz, Elşen Aydın, and Shojaa Zaher Abusakha.

I want to express my deepest appreciation to my family. Their endless love, patience, and encouragement have been my greatest motivation. This journey would not have been possible without your unconditional support.

Lastly, I am incredibly grateful to Merve Yıldız for her patience, understanding, and for providing the motivation and mental support throughout my master's journey.

This research was partially a part of NEXUS Project, which has received funding from the European Union's Horizon Europe research and innovation program under grant agreement No. 101075330.

This research was partially funded by the Scientific and Technological Research Council of Turkey (TÜBİTAK) under the grant number 20AG002.



## TABLE OF CONTENTS

ABSTRACT .....	v
ÖZ.....	vii
ACKNOWLEDGMENTS .....	x
TABLE OF CONTENTS .....	xii
LIST OF TABLES .....	xv
LIST OF FIGURES .....	xvi
LIST OF ABBREVIATIONS .....	xviii
CHAPTERS	
1 INTRODUCTION .....	1
1.1 Solar Cell Operation .....	2
1.1.1 The p-n Junction .....	3
1.1.2 Heterojunctions.....	7
1.1.3 Charge Carrier Recombination.....	7
1.1.4 Surface Passivation.....	10
1.1.5 Solar Cell Parameters .....	12
1.2 Solar Cell Designs .....	14
1.2.1 Aluminum Back Surface Field (Al-BSF) Solar Cells .....	14
1.2.2 Passivated Emitter and Rear Contact (PERC) Solar Cells .....	15
1.2.3 Tunnel Oxide Passivated Contact (TOPCon) Solar Cells .....	15
2 LITERATURE REVIEW .....	17
2.1 AZO:H as a Transparent Conductive Oxide (TCO) and Passivating Layer	17
2.2 MoO <sub>x</sub> as a Hole-Selective Passivating Layer .....	20

3	CHARACTERIZATION METHODS .....	23
3.1	Spectroscopic Ellipsometry (SE) .....	23
3.2	Quasi-Steady-State Photoconductance (QSSPC).....	25
3.3	Characterization of The Optical Properties .....	26
3.3.1	UV-Visible Light Spectroscopy.....	26
3.3.2	External Quantum Efficiency (EQE).....	27
3.4	Electrical Resistance Measurements .....	27
3.4.1	Four-Point-Probe Method .....	27
3.4.2	Cox-Strack Method .....	28
3.4.3	Transfer-Length Method (TLM).....	31
3.5	Scanning Electron Microscopy (SEM) .....	32
4	FABRICATION AND EXPERIMENTAL FLOW .....	35
4.1	Fabrication and Experimental Flow of AZO:H Passivation Contacts .....	35
4.1.1	ALD Process .....	35
4.1.2	Experimental Flow .....	39
4.2	Fabrication and Experimental Flow of MoO <sub>x</sub> Passivating Contacts.....	40
4.2.1	Physical Vapor Deposition (PVD).....	40
4.2.2	Experimental Flow .....	41
5	RESULTS AND DISCUSSION .....	45
5.1	Results for AZO:H .....	45
5.1.1	AZO:H on TOPCon .....	45
5.1.2	Optical Properties.....	47
5.1.3	Structural Properties.....	49
5.1.4	Electrical Properties .....	51

5.2	Results for MoO <sub>x</sub> .....	54
5.2.1	Electrical Properties.....	54
5.2.2	MoO <sub>x</sub> on PERC .....	56
6	CONCLUSION .....	61
	REFERENCES .....	63

## LIST OF TABLES

### TABLES

Table 5.1 Deposition parameters of AZO:H layers on symmetric lifetime samples with corresponding thickness measured by SE.....	45
Table 5.2 The $\rho_c$ results for different MoO <sub>x</sub> thicknesses [56].....	55
Table 5.3 Solar cell parameters of PERC cells utilizing different thicknesses of local MoO <sub>x</sub> /Ag back contacts [56].....	56

## LIST OF FIGURES

### FIGURES

Figure 1.1. The energy band diagram of (A) separate n-type c-Si and p-type c-Si, and (B) when they are brought into contact .....	6
Figure 1.2. A schematic showing the generation and different types of recombination processes across the band gap of a semiconductor.....	8
Figure 1.3 Schematic representation of interface defect densities vs fixed charge densities of the most common passivation layers, adapted from Cuevas et al. [9].	11
Figure 1.4. Schematics of common (A) Al-BSF, (B) mono-facial PERC, (C) mono-facial TOPCon, (D) bifacial PERC, and (E) bifacial TOPCon solar cells .....	14
Figure 3.1. A schematic representation for SE.....	24
Figure 3.2. Representative schematics for (A) the sample design used for Cox-Strack and (B) a simplified sketch showing the current spreading (in red) through the c-Si bulk while the current flows from the top to the bottom contact (spread backside area shown in purple) [56].....	29
Figure 3.3. A schematic showing the current flow path and $L_T$ during a TLM measurement.....	31
Figure 4.1. A schematic representation of the deposition steps of an ALD process .....	36
Figure 4.2. Schematic representation of the separation of precursor and co-reactant in spatial-ALD .....	38
Figure 4.3. 2D schematics of the fabricated samples .....	39
Figure 4.4. Process flow diagram of the fabrication of PERC cells employing local $\text{MoO}_x/\text{Ag}$ back contact, also showing a schematic of the final cell [56] .....	42
Figure 5.1. (A) Change in $iV_{oc}$ and (B) $iV_{oc}$ values of the AZO:H(/ $\text{AlO}_x$ ) stacks deposited on symmetric n-TOPCon samples for different forming gas annealing temperatures .....	46
Figure 5.2. Transmission results for bare glass substrate, 20 nm AZO:H(/ $\text{AlO}_x$ ), 88 nm, and 200 nm AZO:H.....	48

Figure 5.3. Transmission results for varying (A) deposition temperature, (B) DMAI flow, and (C) H <sub>2</sub> O Flow .....	49
Figure 5.4. SEM images of (A) 80 nm and (B) 200 nm AZO:H .....	50
Figure 5.5. Cross-sectional SEM image of 200 nm AZO:H on 200 nm SiO <sub>x</sub> .....	50
Figure 5.6. $R_{Sheet}$ results (A) for different DMAI and H <sub>2</sub> O flows for 20 nm AZO:H deposited at 230°C, and (B) for different thicknesses deposited at 110 and 230°C	52
Figure 5.7. (A) $R_{Sheet}$ and (B) $\rho_c$ values measured by TLM for 20 nm AZO:H deposited and forming gas annealed at different temperatures.....	53
Figure 5.8. The dark I-V results for the test samples with (A) c-Si/Ag without MoO <sub>x</sub> and (B) 5 nm MoO <sub>x</sub> between c-Si and Ag. (C) $R_T - R_{S_{spread}}$ vs (front circular area) <sup>-1</sup> + (spread backside area) <sup>-1</sup> plot for the test sample with 5 nm MoO <sub>x</sub> [56]...	55
Figure 5.9. Change in FF and $\rho_c$ with varying MoO <sub>x</sub> thickness [56].....	57
Figure 5.10. The I-V results under 1-sun for the best-performing PERC solar cell employing 5 nm local MoO <sub>x</sub> /Ag [56] .....	58
Figure 5.11. The quantum efficiency measurements for the best-performing cell with the image of the front surface of the complete solar cell [56] .....	59

## LIST OF ABBREVIATIONS

### ABBREVIATIONS

PV	Photovoltaics
LCOE	Levelized cost of electricity
BoS	Balance of system
c-Si	Crystalline silicon
SRH	Shockley-Read-Hall
AlO <sub>x</sub>	Aluminum oxide
SiN <sub>x</sub>	Silicon nitride
ALD	Atomic layer deposition
PECVD	Plasma-enhanced chemical vapor deposition
ARC	Anti-reflective coating
SiO <sub>x</sub>	Silicon oxide
TOPCon	Tunnel oxide passivated contact
Al-BSF	Aluminum back surface field
PERC	Passivated emitter and rear contact
LID	Light-induced degradation
TCO	Transparent conductive oxide
ZnO	Zinc oxide
AZO:H	Hydrogenated aluminum-doped zinc oxide
MoO <sub>x</sub>	Molybdenum oxide

SHJ	Silicon heterojunction
DEZ	Diethylzinc
DMAI	Dimethylammonium iodide
TMA	Trimethylaluminum
SE	Spectroscopic ellipsometry
SDE	Saw damage etched
QSSPC	Quasi-steady-state photoconductance
EQE	External quantum efficiency
IQE	Internal quantum efficiency
SEM	Scanning electron microscopy
XPS	X-ray photoelectron spectroscopy
Cz	Czochralski
FZ	Float zone
LPCVD	Low-pressure chemical vapor deposition
POCl <sub>3</sub>	Phosphoryl chloride
BDEAS	Bis(diethylamino)silane
PVD	Physical vapor deposition
LCO	Local contact opening



# CHAPTER 1

## INTRODUCTION

Our world faces an escalating climate crisis, with the average global temperature rising by 1.1°C since 1880, mainly driven by ever-increasing greenhouse gas emissions caused by human activities [1]. The largest portion of these greenhouse gases is CO<sub>2</sub>, predominantly from the burning of fossil fuels. Climate change is responsible for the acceleration of Arctic ice loss and extreme weather events such as droughts, floods, storms, wildfires, and heat waves. Ultimately, it endangers human health and survival, vital resources like clean water and food, and the intricate balance of nature. To combat climate change and mitigate the risk of exceeding a 1.5°C average global temperature increase, which could trigger an irreversible ecosystem collapse, it is crucial to drastically alter the energy production methods, shifting away from fossil fuels toward sustainable clean energy production.

Photovoltaics (PV) have emerged as a critical solution to transition to sustainable energy. Between 2010 and 2023, the total globally installed PV systems showed a 35 times increase, positioning PV as the fastest-growing sustainable energy source [2]. This significant growth can be primarily explained by the 90% reduction in the globally weighted average levelized cost of electricity (LCOE) for PV panels during the same period. The main cause of the cost reduction comes from the decreasing module prices. As a matter of fact, the decrease in module prices has been so significant that the balance of system (BoS) costs (including structural components, electrical wiring, installation, and labor costs) now comprise the majority of the total PV system cost, with 61% [2].

Consequently, achieving higher solar cell efficiency becomes more important in order to reduce the total PV system cost. A more efficient cell will generate more

power from the same physical area, meaning fewer modules will be needed to reach the same power output; thus, the BoS cost per power output will be decreased.

In order to maximize the solar cell efficiency, minimizing the carrier recombination by passivation is highly important. While the solar cell operation and the passivation mechanism are more detailedly explained in the later chapters, essentially, passivating involves applying one or more additional thin layers to the surface of the solar cell to heal the imperfections and defects on the surface, and/or generate a voltage difference so that the charge carriers are transported more selectively and effectively. Although each additional thin layer comes with its own complexity and fabrication cost, given the increasing relative contribution of the BoS costs to the total PV system cost, utilizing advanced methods like passivation is vital for the economic sustainability and the widespread adoption of PV.

## **1.1 Solar Cell Operation**

Solar cells are electronic devices that convert sunlight directly into electricity by producing both a voltage and a current. This process is referred to as the photovoltaic effect. Sunlight is absorbed by the absorber material in the solar cell, exciting electrons to a higher energy level. Later, the electrons are guided toward an external load, where they dissipate their energy and then return to the solar cell. Dominantly, semiconductors are used for photovoltaic energy conversion.

A semiconductor is a material that has an electrical conductivity between that of a conductor and an insulator. They have a few electronvolts of band gap ( $E_g$ ) between their conduction and valence bands. This gap partially prevents the electrons from being free and readily participating in a current, unlike a conductor. This gap is smaller than the band gaps of insulators, so that the valence electrons of semiconductors can be excited to energy levels above the band gap by sending energy in the form of heat, light, etc. Photovoltaics uses light as the energy source, so when a photon with energy equal to or higher than the band gap ( $\hbar\omega \geq E_g$ ) of the

used semiconductor is absorbed, an electron jumps up to an energy level above the band gap, leaving an ‘empty spot’ called a “hole”, which is just the absence of an electron. This process is called electron-hole pair generation, and it is the foundation of generating the photocurrent. The holes can be filled by neighboring bonded electrons, in which case a new hole will appear in the place of the neighboring electron, so the holes will seem as if they freely move in the valence band. For this reason, in photovoltaics, the holes are conventionally treated as positively charged quasi-particles for ease of modeling.

Crystalline silicon (c-Si) is the semiconductor material that dominates the photovoltaic market with a market share of about 97% due to its abundance on Earth, relatively low price, non-toxicity, and long-term stability [3]. The Si atom has four valence electrons, and in its crystalline form, each Si atom is connected to four other Si atoms by covalent bonds. c-Si has an indirect  $E_g$  of 1.12 eV, and at room temperature, it absorbs wavelengths between 400-1100 nm, which corresponds to most of the visible light where the solar irradiance peaks. The indirectness of the  $E_g$  signifies that the valence band maximum and the conduction band minimum are located at different positions in momentum space. Therefore, the electron to be excited needs both a phonon (a quantum of lattice vibration) alongside a photon, which results in a relatively low absorption coefficient compared to materials with a direct band gap. Nevertheless, efficient light management methods such as antireflection coatings and surface texturing enable effective light absorption in c-Si [4]. In addition, the indirect band gap means that the radiative recombination of electrons and holes will be inefficient as well, leading to electrons and holes with higher lifetimes.

### **1.1.1 The p-n Junction**

The efficiency with which a solar cell converts light into electricity is critically dependent on two subsequent processes: the effective separation of these photogenerated charge carriers and their subsequent collection at the appropriate

electrical contacts. Without an efficient mechanism for separating electrons from holes, these carriers would rapidly recombine within the semiconductor material, instead of contributing to an electrical current. This highlights the fundamental requirement for an internal electric field to drive the separated carriers towards their respective terminals.

The p-n junction is the primary active region in almost all conventional solar cells, being the basic structure responsible for charge separation. Its principal function is to create an internal electric field that effectively separates photogenerated electron-hole pairs. Prior to the p-n junction, the doping mechanism, a key concept for the formation of such junctions, is explained in the following part.

An important feature of semiconductors is their ability to be doped, which allows for the precise manipulation of the concentration of electrons and holes. In c-Si, doping is typically achieved using atoms with either three or five valence electrons, most conveniently with boron (B) and phosphorus (P). When a P atom is introduced into a c-Si lattice, it replaces one of the Si atoms, and its five valence electrons interact with four neighboring Si atoms. These four electrons form stable bonds, but the fifth electron is easily freed by ambient thermal energy at room temperature, turning into a mobile charge carrier. Essentially, a P atom donates a free electron and becomes positively ionized. Similarly, when a B atom is introduced into the lattice, its three valence electrons form stable bonds with four of its neighboring atoms, leaving one missing bond and consequently creating a mobile hole in the lattice while negatively ionizing the B atom.

Doping with P leads to electrons being the majority charge carriers in the semiconductor, which makes it an n-type semiconductor; on the other hand, doping with B makes the holes the majority charge carriers, turning the semiconductor into p-type. Both n-type and p-type c-Si are charge-neutral when they are isolated since the ionized doping atoms are compensated by the charge carriers. However, when a p-n junction is formed by bringing them in contact with each other, both majority carriers diffuse into the other side, creating a “depletion region” at the junction that

is depleted of mobile carriers. The lack of charge carriers in this region disrupts the charge neutrality by exposing the negatively charged fixed ions in the p-type region and positively charged ones in the n-type region. Eventually, it creates an electric field and a corresponding built-in potential difference ( $V_{\text{built-in}}$ ), which sweeps holes into the p-type region and electrons into the n-type region for efficient charge carrier separation. This  $V_{\text{built-in}}$  determines the band bending at the surface.

The energy band structures of separate p-doped and n-doped c-Si and the band structure when a p-n junction is formed by bringing them into contact are shown in Figure 1.1. Here,  $E_V$ ,  $E_C$ , and  $E_{\text{vac}}$  represent the highest energy level in the valence band, the lowest energy level in the conduction band, and the vacuum energy level, respectively.  $E_{\text{vac}}$  is the energy level just outside the solid, which can be thought of as the required energy for an electron to be removed from the material.

The Fermi level ( $E_F$ ), a fundamental concept in solid-state physics, represents the electrochemical potential of electrons within a material. Formally, it is the thermodynamic work required to add one electron to the system.  $E_F$  represents the energy state that has a 50% probability of being occupied at thermodynamic equilibrium.

The position of  $E_F$  relative to band edges determines the carrier concentration and electrical properties. For an n-type material,  $E_F$  is closer to  $E_C$ , and for a p-type material, it is closer to  $E_V$ . A fundamental rule of thermodynamics dictates that for any system of materials in thermal and electrical contact, the  $E_F$  must be uniform throughout the system at equilibrium. This uniform  $E_F$  is achieved by an electron flow from higher Fermi level material to lower Fermi level material when they are brought into contact until an equilibrium is obtained.

This requirement for a single, constant electrochemical potential is the foundational principle that governs all electronic phenomena at a semiconductor junction, such as band bending and the formation of a depletion region.

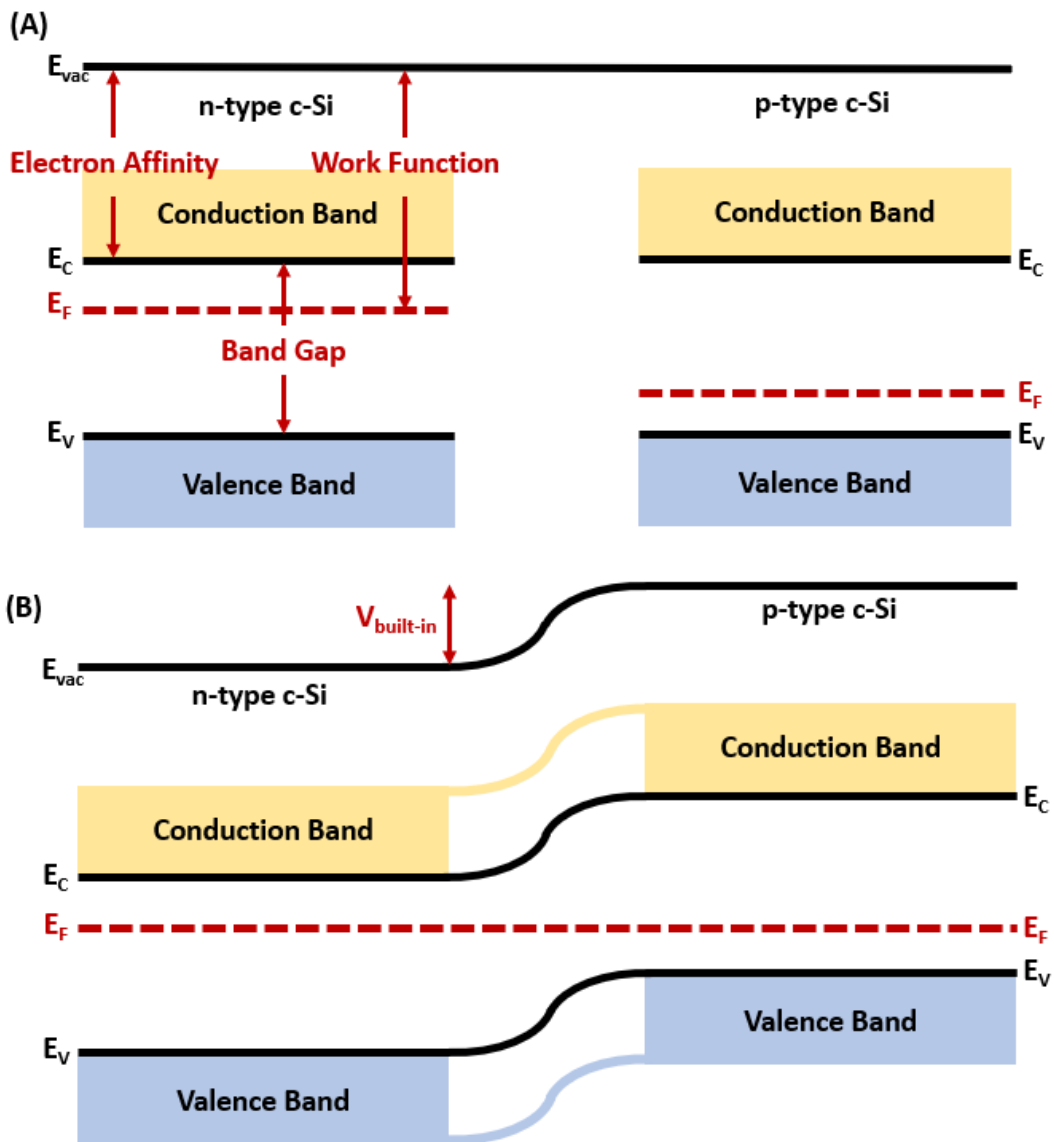


Figure 1.1. The energy band diagram of (A) separate n-type c-Si and p-type c-Si, and (B) when they are brought into contact

The work function is defined as the minimum energy needed to excite an electron from the Fermi level to the  $E_{vac}$ . The electron affinity is the energy between the  $E_{vac}$  and the  $E_C$ . The work function and the electron affinity, together with the  $E_F$ , determine how the energy bands of different materials will align when they are brought into contact.

### 1.1.2 Heterojunctions

A p-n junction formed by bringing a p-type c-Si and an n-type c-Si is essentially a homojunction because they are both the same material with identical intrinsic properties like  $E_g$  and electron affinity. However, when two different semiconductor materials that have different  $E_g$  values and electron affinities are brought together to form a heterojunction, the alignment of their Fermi levels results in offsets, or energy barriers, in the conduction and valence bands.

The difference in the electron affinities primarily determines the conduction band offset,  $\Delta E_C$ . Hence, since  $E_g$  is the difference between  $E_C$  and  $E_V$ , the valence band offset,  $\Delta E_V$ , is identified as

$$\Delta E_V = \Delta E_C - \Delta E_g \quad (1.1)$$

These band offsets can be engineered by the choice of different materials to control the flow of electrons and holes separately, to obtain electron or hole-selective characteristics.

### 1.1.3 Charge Carrier Recombination

Recombination is one of the fundamental mechanisms in semiconductors where an excited electron from the conduction band and a hole from the valence band meet and annihilate each other. The photo-generated electron-hole pairs have to be efficiently separated at the p-n junction and collected through the contacts. Although in reality, some electrons and holes recombine before they are collected and utilized due to certain limitations. The recombination process can severely reduce the photocurrent and the efficiency of the solar cell. In this section, the recombination mechanisms that take place during solar cell operation are explained. Figure 1.2 summarizes the different types of recombination processes across the band gap.

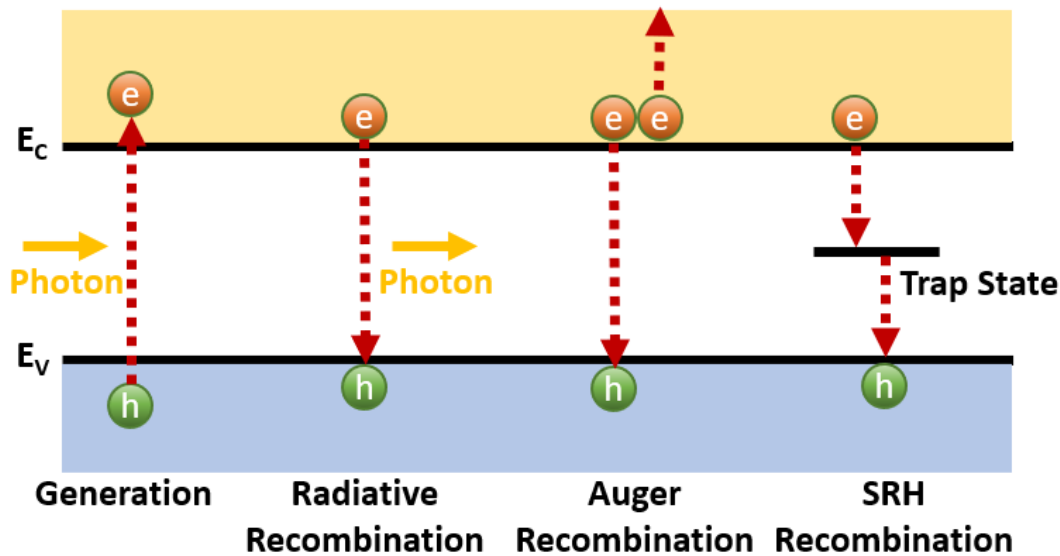


Figure 1.2. A schematic showing the generation and different types of recombination processes across the band gap of a semiconductor

### 1.1.3.1 Direct Recombination

Direct recombination, a band-to-band process, is essentially the opposite of photon absorption. An already excited electron in the conduction band falls into the valence band by filling a hole, and gives up its energy by emitting a photon. While in a direct band gap material, such recombination requires only an electron and a hole, an indirect band gap material like c-Si necessitates the involvement of a phonon in addition to the electron and hole, due to the mismatch between the valence band maximum and conduction band minimum in momentum space. The addition of a phonon turns this mechanism into a three-quasi-particle process and significantly reduces its probability. Therefore, such recombination is usually negligible for indirect band gap materials like c-Si.

### 1.1.3.2 Auger Recombination

In Auger recombination, the excess momentum and energy of a charge carrier are transferred to another charge carrier of the same type, so that the recombination can

happen. If the particle absorbing the energy is an electron, it is excited into higher energy levels and then loses its energy in the form of heat and vibration. Similarly, if it is a hole, it moves into lower energy levels and then loses its energy as vibration. Auger recombination is a three-quasi-particle process; thus, it heavily depends on the charge carrier density. This type of recombination dominates in highly doped regions.

### **1.1.3.3 Shockley-Read-Hall (SRH) Recombination**

SRH recombination, also known as defect recombination, occurs via impurities or trap states located in the band gap [5]. These trap states are products of impurities, crystallographic defects, or dangling bonds in the lattice. When an electron-hole pair is recombined in a trap state, the energy is released primarily as phonons instead of photons. SRH recombination is mostly negligible in today's extremely pure c-Si bulks. It is mostly observed at the surface of the semiconductor and the interfaces. The abrupt termination of the crystal lattice leads to dangling bonds and forms a vast number of surface defects and trap states, which causes a significantly high density of interface states ( $D_{it}$ ). These interface states act as alternative routes for charge carriers to recombine. The surface recombination is the primary mechanism for carrier loss and limits the efficiency of the solar cell.

Reducing the surface recombination is critical to reach high-efficiency solar cells. It can be reduced either by excessively doping the surface so that the minority carrier concentration can be reduced near the surface, or by passivating the surface by depositing a thin film. Although the first case used to be historically common, it significantly increases the Auger recombination and limits the efficiency [6]. Therefore, in order to reduce the SRH recombination at the semiconductor surface without causing significant Auger recombination, various passivating layers are employed in modern solar cell designs.

### 1.1.4 Surface Passivation

The surface passivation is applied to reduce the recombination near the semiconductor surface. The high recombination rate at the surface is mainly a consequence of dangling bonds at the surface, which create alternative paths for electrons and holes to recombine. In order to diminish the rapid recombination at the surface, two types of passivation mechanisms can be utilized:

- **Chemical Passivation:** This type of passivation involves neutralizing the dangling bonds by introducing another atomic species or by depositing a thin layer onto the surface. These introduced atoms create bonds with the surface layer, effectively tying the dangling bonds up and reducing the trap states or the  $D_{it}$ .
- **Field-Effect Passivation:** Field-effect passivation, also known as electrical passivation, creates an electric field near the surface to repel the minority carrier away from the surface. The electric field is generated by the fixed charges of a passivation layer or by heavy doping. Instead of reducing the  $D_{it}$ , it reduces the minority carrier density near the surface, so the recombination becomes less probable.

Various types of materials can be used to realize either or both of these passivations. Aluminum oxide ( $AlO_x$ ) and silicon nitride ( $SiN_x$ ) are two of the most popularly used ones.  $AlO_x$  is typically deposited by atomic layer deposition (ALD), typically on the back surface of p-type c-Si solar cells. Its negative fixed charges create a field-effect at the surface, repelling minority carrier electrons away.  $SiN_x$  is commonly deposited by plasma-enhanced chemical vapor deposition (PECVD). Even though it is mostly used as an anti-reflective coating (ARC) layer, it also provides field-effect passivation, reducing surface recombination. These layers are also hydrogen-rich, that is, they contain high numbers of hydrogen atoms after they are deposited. When they are annealed at high temperatures, they release their hydrogen into the semiconductor surface. The hydrogen atoms bond with dangling bonds and provide extra chemical passivation. Using hydrogen atoms as a means of passivation is called

“hydrogenation”, which is an important process in order to reduce the  $D_{it}$  levels near the semiconductor surface. Hydrogenation can also be provided by annealing the semiconductor in  $H_2$  or forming gas (a mixture of hydrogen and nitrogen) ambient.

Silicon oxide ( $SiO_x$ ) is another passivating layer that has been commonly used for its great chemical passivation. It has been shown that the  $D_{it}$  values can be reduced to an order of  $10^9 \text{ cm}^{-2}$  after annealing c-Si passivated with  $SiO_x$  and a sacrificial  $AlO_x$  capping [7].  $SiO_x$  is commonly used together with doped poly-Si layers in the so-called tunnel oxide passivated contact (TOPCon) structure [8]. Although this structure results in excellent surface passivation, doped poly-Si causes parasitic absorption, a concept where some of the photons are absorbed in a layer above the semiconductor bulk, so the generated electron-hole pairs recombine back before they can be effectively separated. In Figure 1.3, a schematic representation of the interface properties of these layers is given.

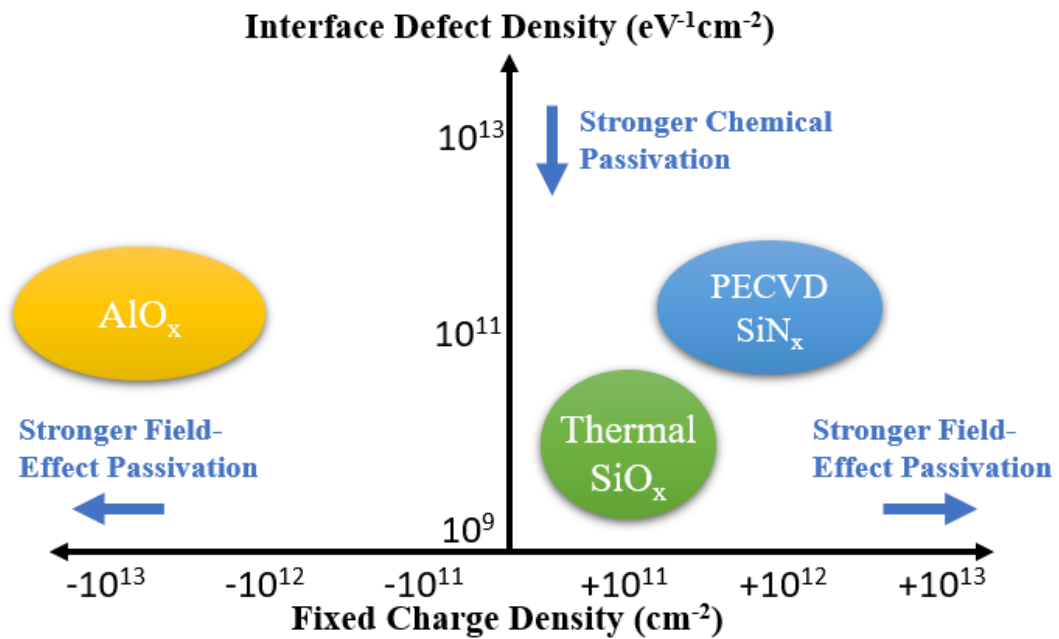


Figure 1.3 Schematic representation of interface defect densities vs fixed charge densities of the most common passivation layers, adapted from Cuevas et al. [9]

These passivating thin films are used in various stack combinations. Since these layers are generally insulators, they are incorporated into different designs so that they can passivate the c-Si surface without completely blocking the current transport into the metal contact. These designs most commonly include methods such as:

- depositing the film extremely thin, enabling current transport via tunneling and through pinholes [10];
- applying the films locally on the c-Si surface [11]; or
- opening tiny windows through the passivating insulating layer to form local contacts between metal and c-Si [12].

When a passivation layer allows for charge transport, either through tunnelling or by being inherently conductive, it can then function as a passivating contact. A passivating contact is, essentially, a layer that simultaneously passivates the surface and participates in current transport. Their  $E_g$  and work function induce a band alignment with Si and metal in such a way that these layers allow one type of charge carrier to be transported; hence, they provide carrier-selectivity.

In addition to providing excellent surface passivation, a carrier-selective passivating contact should minimize the contact resistivity ( $\rho_c$ ).  $\rho_c$  describes the electrical resistance at the interface between the semiconductor and the metal contact. Low  $\rho_c$  is vital for the efficient extraction of the majority carriers to the external circuit.

In conclusion, a good passivating and carrier-selective contact is responsible for minimizing the recombination current density ( $J_0$ ) by achieving superior passivation quality, which directly contributes to open-circuit voltage ( $V_{oc}$ ), and minimizing  $\rho_c$  by successfully conducting the current to the external circuit with low resistive losses, which translates into high fill factor (FF).

### **1.1.5 Solar Cell Parameters**

Solar cell performance is quantitatively evaluated using key device parameters derived from their current-voltage (I-V) characteristic curves. These parameters are

fundamental for evaluating how efficiently a solar cell converts incident sunlight into electrical energy and are crucial for analyzing potential issues within the cell structure or materials.

#### **1.1.5.1 Open-Circuit Voltage ( $V_{oc}$ )**

$V_{oc}$  is the maximum voltage that a solar cell can produce when no external load is connected. It mainly serves as an indicator of passivation quality. It is highly sensitive to recombination; therefore, a high  $V_{oc}$  is typically accompanied by a low  $J_0$ .

#### **1.1.5.2 Short-Circuit Current Density ( $J_{sc}$ )**

$J_{sc}$  represents the maximum current density ( $I_{sc}/\text{cell area}$ ) that flows through a solar cell when the voltage across it is zero. It mainly serves as an indicator of the device's ability to capture and effectively utilize the incident solar spectrum. A high  $J_{sc}$  is achieved by maximizing the photon absorption and minimizing carrier losses due to recombination or parasitic absorption of front layers.

#### **1.1.5.3 Fill Factor (FF)**

FF is a dimensionless parameter that quantifies the squareness of the J-V curve. It is defined as the ratio of the extracted maximum power from the cell to the theoretical maximum power. It primarily indicates the resistive losses throughout the device.

#### **1.1.5.4 Power Conversion Efficiency (PCE)**

The efficiency of a solar cell is the vital overall parameter that represents the percentage of incident solar power that is being converted into electrical power by the solar cell. It is calculated as

$$\text{PCE} = \frac{V_{oc} J_{sc} FF}{P_{in}} \quad (1.2)$$

where  $P_{in}$  is the incident solar power.

## 1.2 Solar Cell Designs

The advancement of standard crystalline silicon solar cell technology reflects an ongoing development aimed at overcoming limits while improving performance, mainly through enhanced passivation and contact strategies.

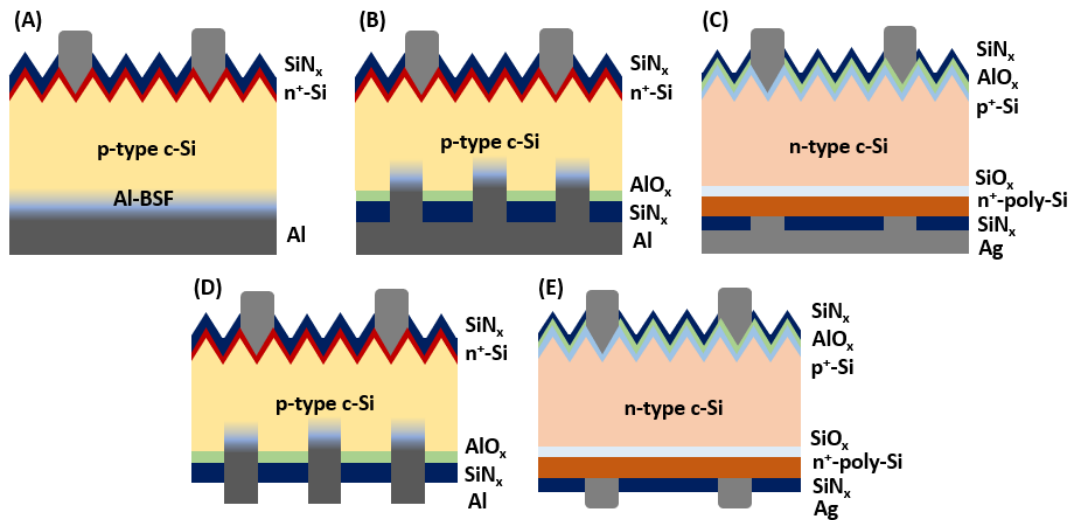


Figure 1.4. Schematics of common (A) Al-BSF, (B) mono-facial PERC, (C) mono-facial TOPCon, (D) bifacial PERC, and (E) bifacial TOPCon solar cells

### 1.2.1 Aluminum Back Surface Field (Al-BSF) Solar Cells

The Al-BSF cell was considered the "standard solar cell" in the industry for a long time. In this design, the silicon wafer's entire back surface is covered with an aluminum layer (Figure 1.4A). During the high-temperature firing, aluminum diffuses into the silicon and creates a heavily doped  $p^+$  region, known as the back surface field. This electric field at the rear surface assists in preventing minority carrier electrons from recombining at the back contact. Al-BSF cells were effective

for their period, but their maximum efficiency was constrained by a less effective direct metal/semiconductor back contact, which introduces a large number of  $D_{it}$ . This resulted in larger recombination losses at the back surface.

### **1.2.2 Passivated Emitter and Rear Contact (PERC) Solar Cells**

PERC technology marked a significant advancement, rapidly superseding Al-BSF cells and achieving market dominance, with almost 70% market share by 2023 [3]. The core innovation in PERC cells is the introduction of a dielectric passivation layer, typically composed of  $AlO_x$  or  $SiN_x$ , on the rear surface, beneath the metal contacts (Figure 1.4B & 1.4D). This passivation layer stack substantially reduces surface recombination losses through both chemical passivation and field-effect passivation by substantially reducing the total surface area exposed to direct metal/semiconductor contact. Additionally,  $SiN_x$  functions as an internal rear reflector, directing unabsorbed light back into the silicon wafer, thereby improving photon absorption and enhancing both  $V_{oc}$  and  $J_{sc}$ . PERC modules typically achieve efficiencies near 21% with single cell efficiencies reaching 24% [3,13]. However, PERC cells suffer from light-induced degradation (LID), which can cause their efficiency to diminish over time. Additionally, the reliance on metal/semiconductor contacts at the rear side fundamentally limits the maximum efficiency of this structure. Although the PERC design currently dominates the PV market, it is steadily getting replaced by other advanced passivation designs, mainly TOPCon.

### **1.2.3 Tunnel Oxide Passivated Contact (TOPCon) Solar Cells**

TOPCon technology, which is now gaining a lot of popularity and starting to push PERC cells out of the market, is the next evolutionary step in crystalline silicon solar cells. By adding an ultra-thin  $SiO_x$  layer (about 1-2 nm thick) and a poly-Si layer, TOPCon cells expand on the PERC concept by completely removing the metal/semiconductor interface (Figure 1.4C & 1.4E). Usually applied to both the

front and rear surfaces, this "tunnel oxide passivated contact" arrangement allows for extremely selective carrier extraction with  $J_0$  values below 10 fA/cm<sup>2</sup> [14], with their module efficiencies reaching 22.5% [3]. The lab-scale solar cells utilizing TOPCon design show remarkable efficiencies up to 26% [15]. In addition to offering superior passivation that reduces recombination losses for minority carriers, the ultra-thin tunnel oxide layer enables majority carriers to "tunnel" through to the polysilicon layer with low resistance, reducing the contact resistivity and the resistive losses. The performance and lifetime of cells are greatly enhanced by this dual role. Advantages of TOPCon cells include excellent thermal performance, with minimal performance degradation at high temperatures, and high resistance to degradation mechanisms like LID due to employing n-type c-Si as the bulk instead of p-type.

## CHAPTER 2

### LITERATURE REVIEW

#### 2.1 AZO:H as a Transparent Conductive Oxide (TCO) and Passivating Layer

Zinc Oxide (ZnO) thin films, both as intrinsic and doped, are widely recognized as a TCO layer, employed mostly on silicon heterojunction (SHJ) solar cells, and have also been recently recognized for their ability to passivate the c-Si surface [16,17]. The commonly used passivation layers, as discussed earlier, are either insulating (such as  $\text{AlO}_x$ ,  $\text{SiN}_x$ ,  $\text{SiO}_x$ ) or not transparent and result in parasitic absorption (such as poly-Si). Therefore, a passivating transparent and conductive material like ZnO has great potential as a passivating contact. The conductivity of ZnO is generally improved by doping with various elements, like boron [18], indium [19], and most commonly aluminum [20–22] to introduce extra charge carriers. In this thesis, we will focus on aluminum-doped ZnO (AZO).

When ZnO is doped with Al, the Al ions substitute for Zn ions. Al has one more valence electron than the Zn ions, so this substitution provides one extra free electron, increasing the carrier concentration and improving the conductivity. AZO can be deposited by various methods, such as temporal and spatial ALD [23,24], sputtering [25], and the sol-gel method [26]. Later, AZO can be hydrogenated to form hydrogenated AZO (AZO:H) with various methods to provide a better passivating quality, if it was not already simultaneously hydrogenated during the deposition. Both AZO:H and ZnO are polycrystalline materials that tend to grow in a hexagonal wurtzite crystal structure predominantly along the c-axis for the (002) plane, meaning their growth is perpendicular to the substrate surface [27]. It was observed that doped ZnO results in more oriented crystals, improving the resistivity [28].

The electron affinity of AZO:H is about 4.4 eV, and its work function (around 4.07-4.12 eV depending on the doping rate [29]) is below the work function of c-Si; hence, it keeps the holes away from the surface, applying an electron-selective characteristic along with the field-effect passivation [22]. The  $E_g$  of the AZO:H typically falls between 3.22-3.64 eV [29]. This  $E_g$  is highly dependent on the doping level due to the Burstein-Moss effect, where the apparent  $E_g$  of a material increases due to the lowest energy levels in the conduction band being fully occupied (or the highest energy levels of the valence band for p-type materials), effectively increasing the energy required to overcome the  $E_g$  and making the layer more transparent for shorter wavelengths [22,30]. In addition, AZO:H has a refractive index between 1.80 and 2, making the layer also suitable for use as an ARC.

The electrical resistivity is a key property for any TCO. For high-quality AZO:H layers, resistivities between  $10^{-3}$  to  $10^{-4}$   $\Omega\text{cm}$  are typically achieved, which are sufficiently low for most solar cell applications [31]. The sheet resistance ( $R_{Sheet}$ ), which is the parameter that determines the lateral conduction loss of a layer, is highly dependent on the thickness of the AZO:H layers. Values between 100-250  $\Omega/\text{sq}$  are reached with  $>100$  nm AZO:H layer, while 40 nm thin AZO:H layers can result in 1150  $\Omega/\text{sq}$  [32,33].

When the AZO:H is brought into contact with n-type poly-Si, their similar electron affinities (both at around 4 eV) align well with each other, leading to conduction bands at similar energy levels with a small energy barrier [34]. However, the large difference between their  $E_g$  (3.22-3.64 eV for AZO:H, 1.12 eV for Si) results in their valence bands having a large energy difference. Additionally, the similar work function of AZO:H and n-type poly-Si induces minimal band bending near the surface, leaving a large asymmetry with the small energy barrier at the conduction band and a large barrier at the valence band [34–36]. This significant energy barrier asymmetry facilitates electron transport while impeding hole transport, rendering the AZO:H electron-selective for Si.

On the other hand, in the structures employing AZO:H, the chemical passivation is not achieved solely by the AZO:H layer itself. Generally, a thin interfacial SiO<sub>x</sub> is grown thermally, chemically, or by UV/O<sub>3</sub>, or to simplify the fabrication steps, the native SiO<sub>x</sub> grown during the RCA cleaning of the wafers is used directly to chemically passivate the c-Si surface [17,21,24]. Among these different SiO<sub>x</sub> layers, UV/O<sub>3</sub> and RCA SiO<sub>x</sub> lead to the best passivation qualities. This passivation quality is later significantly improved by a vital post-deposition annealing process, commonly a forming gas anneal (FGA) at temperatures between 400-500°C [37]. Forming gas is a mixture of N<sub>2</sub> and H<sub>2</sub>, typically about 95% to 5% respectively. During the process of FGA, the molecular H<sub>2</sub> dissociates into atomic hydrogen. These hydrogen atoms diffuse through AZO:H to the c-Si/SiO<sub>x</sub> interface and further passivate the remaining defects and dangling bonds.

In order to achieve excellent passivation, the FGA step is realized with a sacrificial AlO<sub>x</sub> capping layer on top of AZO:H. It was observed that without a capping layer, hydrogen starts effusing from the AZO:H layer before the interlayer reaches the peak passivation [17,21]. This sacrificial AlO<sub>x</sub> layer can then be chemically etched using a Na<sub>2</sub>CO<sub>3</sub> solution [24].

The symmetrical n-type c-Si/SiO<sub>x</sub>/AZO:H structures in literature result in impressive peak  $iV_{oc}$  values of about 740 mV, with solar cells employing SiO<sub>x</sub>/AZO:H rear passivating contact achieving 23.17% efficiency on small area cells [29,38].

The combination of transparency, conductivity, and electron-selective passivating properties puts AZO:H in a unique position, opening the door for future designs where AZO:H can be employed as a passivating TCO, ARC, or recombination junction for tandem solar cell applications. Although AZO:H is extensively used as a passivating contact on c-Si with various interfacial SiO<sub>x</sub>, its interaction with poly-Si remains largely unexplored. This research area is critical, as poly-Si is the key component of TOPCon solar cells, the emerging industrial standard. The AZO:H part of this thesis is focused on this important research gap, to investigate the synergy of AZO:H and n-type poly-Si.

## 2.2 MoO<sub>x</sub> as a Hole-Selective Passivating Layer

Molybdenum oxide (MoO<sub>x</sub>) is the sub-stoichiometric form of MoO<sub>3</sub>, where the ratio of oxygen to molybdenum,  $x$ , is typically less than 3 and higher than 2. This oxygen deficiency is the source of conductivity in MoO<sub>x</sub> layers, distinguishing them from stoichiometric MoO<sub>3</sub>, which is an insulating material [39]. This characteristic behavior is observed because the oxygen deficiency in MoO<sub>x</sub> leads to the formation of oxygen vacancy-derived defect energy states in the large band gap, below the minimum of the conduction band. These defect states reach up to the Fermi level, making the material semi-metallic and enabling charge carrier transport through these defect states [40,41]. The sub-stoichiometry of MoO<sub>x</sub> arises during the low-temperature deposition of the source MoO<sub>3</sub> by thermal evaporation or sputtering [41].

The MoO<sub>x</sub> has an  $E_g$  of 3-3.35 eV, which makes the layer transparent for the vast majority of the useful solar spectrum for c-Si solar cells [42]. This is useful for front surface applications of MoO<sub>x</sub> since it will not lead to parasitic absorption.

One of the most vital properties of MoO<sub>x</sub> that determines its hole-selective characteristic is its exceptionally high work function above 5 eV [43]. This high work function is the main reason that enables MoO<sub>x</sub> to induce strong band bending at the c-Si surface. Its work function heavily depends on the oxygen/molybdenum ratio, with more stoichiometric films exhibiting a larger work function [44]. Therefore, introducing a trade-off between the hole-selectivity and conductivity. The MoO<sub>x</sub> films employed as hole-selective layers need to strike a balance where they are conductive enough not to introduce significant resistance, yet stoichiometric enough to keep their high work function. Common MoO<sub>x</sub> hole-selective layers on p-type c-Si may simultaneously exhibit a significantly low  $\rho_c$  of about 0.2 m $\Omega$ cm<sup>2</sup> with a moderate  $J_0$  of 200 fA/cm<sup>2</sup> [41].

The hole selectivity of MoO<sub>x</sub> on p-type c-Si can be understood by considering the alignment of their energy bands upon contact. In the initial state before contact, the

Fermi level of the p-type c-Si lies close to the valence band. The work function of  $\text{MoO}_x$  is larger than the p-type c-Si; therefore, its Fermi level is at a lower energy than c-Si relative to the vacuum level. When they are brought into contact, the Fermi levels must be aligned through the flow of the electrons of the smaller work function c-Si to the higher work function  $\text{MoO}_x$  until the electrochemical potential is constant throughout the system. The lack of electrons near the surface will result in c-Si energy bands bending upward, bringing the valence band even closer to the Fermi level. This leads to an “*accumulation*” of holes on the p-type c-Si surface, turning the surface into a  $p^+$ -region, forming an accumulation layer [42,45,46]. Likewise, for the case of  $\text{MoO}_x$  brought into contact with an n-type c-Si, again due to the higher work function of  $\text{MoO}_x$ , the electrons at the surface will flow to  $\text{MoO}_x$  and expose positively charged fixed ions, depleting the region of electrons. Due to heavy upward band bending, the n-type c-Si at the surface will effectively turn into a p-type region since the valence band gets closer to the Fermi level [44,47].

This strong upward band bending at the c-Si surface attracts holes while pushing away the electrons, hence resulting in hole selectivity. The holes at the c-Si surface tunnel into and through the network of defect energy states located in the  $\text{MoO}_x$  band gap, to be collected [48].

Alongside providing field-effect passivation by shielding the surface from electrons,  $\text{MoO}_x$  also provides chemical passivation by unintentionally forming an interfacial  $\text{SiO}_x$  at the  $\text{MoO}_x/\text{c-Si}$  interface [42,49]. The thin  $\text{SiO}_x$  layer is simultaneously formed during the  $\text{MoO}_x$  deposition and reduces the  $D_{it}$  at the highly defective c-Si surface. Therefore, the overall passivation quality of the  $\text{MoO}_x$  layer is a synergistic outcome of the strong field-effect passivation provided by  $\text{MoO}_x$  and the chemical passivation from the interfacial thin  $\text{SiO}_x$ .

However, the passivation quality of  $\text{MoO}_x$ , along with its excellent hole-selectivity, strongly degrades when this layer is exposed to high-temperature processes such as annealing, mainly due to the reduction of the work function of  $\text{MoO}_x$  and thickening of the interfacial  $\text{SiO}_x$ .  $\text{MoO}_x$  showed reduced  $V_{oc}$  and  $J_{sc}$  after annealing under  $\text{N}_2$ ,

even at temperatures as low as 160 °C [50]. Although depositing MoO<sub>x</sub> on pre-grown thermal SiO<sub>x</sub> slightly increased its thermal stability to withstand temperatures up to 250°C [51], it is nevertheless preferable to integrate MoO<sub>x</sub> into structures in a way that avoids subsequent thermal processing.

The MoO<sub>x</sub> layer is commonly employed on the front side of SHJ structures as a hole-selective layer, resulting in solar cells exceeding 23.8% efficiencies [52]. Due to its popularity on SHJ, MoO<sub>x</sub> is typically used on structures with n-type c-Si bulk [52,53]. There are a few studies integrating MoO<sub>x</sub> into the industrial workhorse p-type PERC-like structures as rear passivation. Depositing full-area MoO<sub>x</sub>/Ag hole-selective contacts on industrial-size p-type solar cells resulted in 17.65% efficiencies with a relatively low  $V_{oc}$  of 626 mV [49]. Low  $V_{oc}$  is mainly due to insufficient chemical passivation provided by the full-area MoO<sub>x</sub>. Depositing MoO<sub>x</sub> as local rear contacts through AlO<sub>x</sub>/SiN<sub>x</sub> rear-passivation stack resulted in 20.4% efficiency with improved 658 mV  $V_{oc}$  on non-industrial small-area high-quality float zone (FZ) wafers [54]. In this thesis, the high-potential local MoO<sub>x</sub> back contact design was implemented on industrial-size PERC solar cells, prepared by industrial processes and precursors.

## CHAPTER 3

### CHARACTERIZATION METHODS

This chapter describes the characterization methods used to examine the optical, electrical, and physical characteristics of AZO:H and MoO<sub>x</sub> thin films deposited in this work. Each section briefly overviews the fundamental principles of the methods and explains how these methods were utilized in this study.

#### 3.1 Spectroscopic Ellipsometry (SE)

SE is a non-destructive and non-contact method, vital for a better understanding of the thin film thickness and optical properties such as refractive index and extinction coefficient. During the operation of SE, a beam of light with typically linear polarization is sent to a sample surface at an incident angle from a polarizer, reflected from the sample surface, becomes elliptically polarized, and collected in the analyzer.

The polarization of the light beam can be separated into two perpendicular components. These are the p-polarized component that is parallel to the plane of incidence and the s-polarized component that is perpendicular to the plane of incidence (Figure 3.1). After the light is reflected from the surface, both these components will undergo a phase shift. The phase shift for p-polarized and s-polarized components can be different, so a parameter named delta ( $\Delta$ ) can be defined as the change in the phase differences between p-polarized and s-polarized components before and after the reflection.

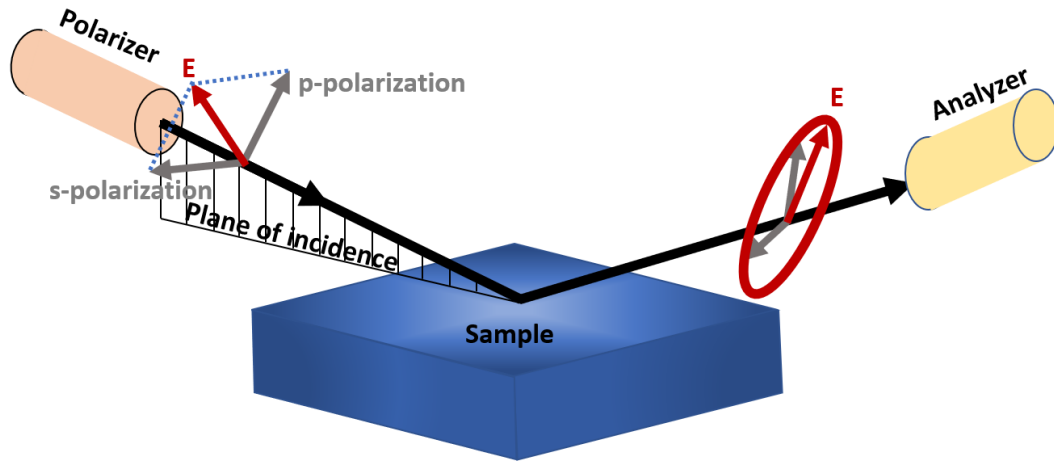


Figure 3.1. A schematic representation for SE

Additionally, after the reflection, the amplitudes of p-polarized and s-polarized components will also be reduced by a different amount. The total reflection coefficients for p-polarized ( $R_p$ ) and s-polarized ( $R_s$ ) components are defined as the ratio of the amplitudes of the light wave before and after the reflection. Psi ( $\Psi$ ) is a parameter corresponding to an angle, whose tangent gives the ratio of the magnitudes of  $R_p$  and  $R_s$ , shown as

$$\tan \Psi = \frac{|R_p|}{|R_s|} \quad (3.1)$$

The fundamental equation of ellipsometry, which is the complex ratio of  $R_p$  and  $R_s$ , can be written as

$$\frac{R_p}{R_s} = \tan \Psi e^{i\Delta} \quad (3.2)$$

The analyzer of the SE measures  $\Psi$  and  $\Delta$ . Later, these parameters are fitted to existing mathematical models depending on the properties of the thin film that is being analyzed [55].

The SE measurements give accurate results even for a few nanometer-scale thin films due to the high sensitivity of the parameter  $\Delta$ . However, the measurements are highly

sensitive to surface roughness and require extremely flat surfaces with uniform thickness inside the measurement spot.

In this thesis, GES5E-Semilab Sopra SE was used on saw damage etched (SDE) and polished samples. Thicknesses of all the deposited thin films were measured by SE. For AZO:H, the Tauc-Lorentz model with Drude oscillators was used [17], and for MoO<sub>x</sub> samples, the Cauchy with Urbach Tail model was used for fitting [49].

### 3.2 Quasi-Steady-State Photoconductance (QSSPC)

The minority carrier lifetime is the typical time it takes for minority carriers to recombine after their excitation. It identifies the quality of the semiconductor bulk as well as the passivation quality on the surface. The effective lifetime ( $\tau_{eff}$ ) includes the lifetime values corresponding to the intrinsic lifetime ( $\tau_{intrinsic}$ ) for carriers recombining due to Auger and radiative recombination, SRH lifetime ( $\tau_{SRH}$ ) for SRH recombination at bulk, and surface lifetime ( $\tau_{surface}$ ) for the surface recombination. Mathematically, it can be represented as

$$\frac{1}{\tau_{eff}} = \frac{1}{\tau_{intrinsic}} + \frac{1}{\tau_{SRH}} + \frac{1}{\tau_{surface}} \quad (3.3)$$

The effective lifetime is commonly measured by using a Sinton Instrument WCT-120. During the measurement, the semiconductor sample is placed on an inductive coil that forms one arm of a radio-frequency (RF) bridge circuit. The sample is momentarily illuminated by a flash of light. The flash of light generates excess charge carriers ( $\Delta n$ ), which increases the photoconductance, and this leads to a change in the impedance of the coil underneath the sample. The change in impedance creates an imbalance in the RF bridge, producing an output voltage. The output voltage can be converted into an absolute measure of photoconductance by calibrating the measurement using samples with known conductance. Later,  $\Delta n$  can be calculated using the wafer thickness and carrier mobilities.  $\Delta n$  is related to the change in photoconductance ( $\sigma_L$ ) as

$$\Delta n = \frac{\sigma_L}{qW(\mu_p + \mu_n)} \quad (3.4)$$

where  $q$  represents the electric charge,  $W$  is the thickness of the semiconductor, and  $\mu_p$  and  $\mu_n$  are the mobility of holes and electrons, respectively. The effective lifetime can then be measured by equation 3.5 after the photogeneration rate ( $G$ ) is measured, again, by the same device.

$$\tau_{eff} = \frac{\Delta n}{G - \frac{d\Delta n}{dt}} \quad (3.5)$$

The principal application of QSSPC in this thesis is the quantitative evaluation of surface passivation quality realized by AZO:H and MoO<sub>x</sub> thin layers.

### 3.3 Characterization of The Optical Properties

#### 3.3.1 UV-Visible Light Spectroscopy

UV-visible light spectroscopy is a fundamental analytical method for determining a material's optical characteristics, particularly transmission, reflection, and absorption. A standard UV-visible light spectroscopy is made up of a broadband light source, a photodetector, a sample holder, and a dispersive part, such as a diffraction grating, to select monochromatic light.

During a transmission measurement, the transmittance is calculated by taking the ratio of the intensity of a monochromatic light beam that passes through the sample to the intensity of another beam that passes through a reference. Similarly, the reflection is measured by comparing the light intensity reflected by the sample to the intensity of the reference light. In this work, the UV-visible light spectroscopy was used to measure the transmittance of the AZO:H and MoO<sub>x</sub> thin films.

### **3.3.2 External Quantum Efficiency (EQE)**

EQE is used for completed solar cell devices to measure their ratio of the number of charge carriers collected in an external circuit to the number of photons of different wavelengths sent upon the front surface of the solar cell. Ultimately, EQE indicates how efficiently a solar cell turns incident photons into useful current for varying wavelengths.

The EQE spectrum is a powerful tool for understanding the performance loss mechanism in the solar cell. Losses in the short wavelength region indicate a potential parasitic absorption by the layers on the front surface of the cell, or high recombination near the front surface. On the other hand, losses in the long wavelength region indicate incomplete light absorption or inefficient collection of the charge carriers that were generated deep in the bulk of the cell.

The EQE measurement includes both electrical and optical losses since it compares the carriers collected by the solar cell to the total number of sent photons. The EQE is often realized with reflection and transmission measurements to exclude the photons that are not absorbed by the solar cell. This is called the internal quantum efficiency (IQE), which is the ratio of the number of charge carriers collected in an external circuit to the number of photons absorbed by the solar cell.

In this thesis, EQE and IQE measurements were taken for fabricated PERC cells employing rear  $\text{MoO}_x$  passivating contacts. EQE, IQE, and UV-visible measurements were conducted using a BENTHAM PVE300 tool.

## **3.4 Electrical Resistance Measurements**

### **3.4.1 Four-Point-Probe Method**

The four-point-probe measurements are commonly used to measure the sheet resistance ( $R_{Sheet}$ ) of the thin-films or doped c-Si surface. The measurement tool is

made up of four parallel, equally spaced probes. These probes are brought into contact with the sample surface. A current is sent from one outer probe to the other while the two inner probes measure the voltage. The  $R_{Sheet}$  is given by

$$R_{Sheet} = \frac{\pi}{\ln 2} \frac{V}{I} \approx 4.532 \frac{V}{I} \quad (3.6)$$

For the four-point-probe measurements, the thickness of the film should be much smaller than the probe spacing. The sample should be square-shaped and large enough to overcome edge effects. If these conditions are not realized, then Equation 3.6 must be used with the appropriate correction factors. Another important point that needs to be considered is the substrate underneath the thin film. For accurate measurements, the thin film must be more conductive than the layers underneath; otherwise, the current will flow through the more conductive layer instead of the thin film. In order to prevent this problem, the AZO:H layers were deposited on square-shaped insulating glass substrates for the accurate extraction of  $R_{Sheet}$ .

### 3.4.2 Cox-Strack Method

The Cox-Strack method is used to measure the  $\rho_c$ , that is, the resistivity between the semiconductor and the metal contact. When the passivating contacts are present between the semiconductor and the metal, their resistive effects are also included in the measured  $\rho_c$ .

During the Cox-Strack measurements, current passes from a top contact through the bulk of the sample to a full-area back contact. The front contacts of the test structure involve circular contacts of different sizes, as shown in Figure 3.2 (A).

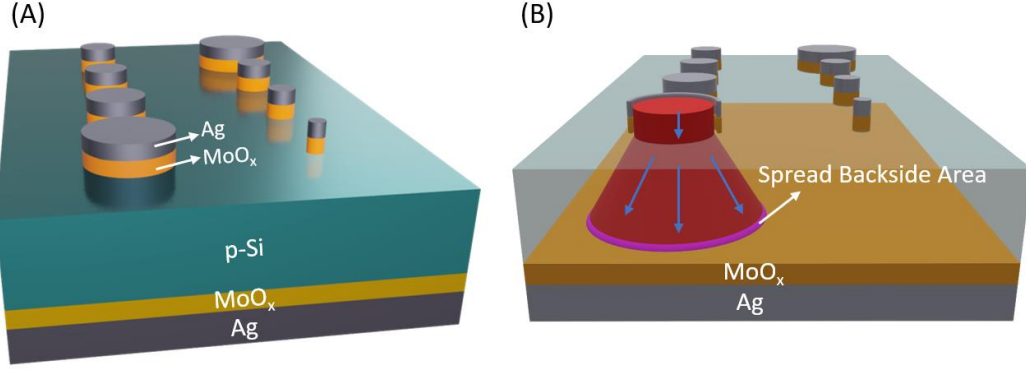


Figure 3.2. Representative schematics for (A) the sample design used for Cox-Strack and (B) a simplified sketch showing the current spreading (in red) through the c-Si bulk while the current flows from the top to the bottom contact (spread backside area shown in purple) [56]

In the Cox-Strack method [57], current is sent from the front circular contact to the back contact in the dark, and the total resistance  $R_T$  is measured for different voltage values. The components of the measure  $R_T$  can be written as

$$R_T = R_c + R_{Spread} + R_0 \quad (3.7)$$

$$R_c = \frac{\rho_c}{\text{front circular area}} = \frac{\rho_c}{\frac{\pi d^2}{4}} \quad (3.8)$$

$$R_{Spread} = \frac{\rho_w}{2d} B \quad (3.9)$$

where  $R_c$  is the contact resistance that includes both the interface resistances (at contact metal/passivating layer/c-Si) and the bulk resistances of the contact metal and the passivating layer.  $R_{Spread}$  is called the spreading resistance and represents the resistance applied to the current while it spreads horizontally in the c-Si bulk.  $\rho_w$  is the bulk resistivity of the semiconductor,  $d$  is the diameter of the front circular contacts, and  $B$  is called the geometrical factor that models the spatial spreading of the flowing current.  $R_0$  is the residual resistance, which includes the resistive effects of back contact and the probe, both of which are independent of the contact area. The

resistance applied by the metal bulk is omitted in Equation 3.7 since it is significantly smaller than all the other components.

In this thesis, an extended version of Cox-Strack (recently proposed by Folchert and Brendel [58]) was used, which enables extracting  $\rho_c$  from symmetric lifetime samples. Due to samples being symmetric, a new resistance component  $R_{Back}$ , backside contact resistance, was introduced as a replacement for  $R_0$  in Equation 3.9.  $R_{Back}$  corresponds to the contact resistance applied by the passivation layer at the back of the symmetric sample as

$$R_{Back} = \frac{\rho_c}{\text{spread backside area}} \quad (3.10)$$

Notice that the backside contact resistance term does not consider the whole back surface area, only the area where the current is able to spread at the back surface of c-Si. A simplified drawing of the current spreading in the c-Si bulk while flowing into the back surface, and the spread backside area was depicted in Figure 3.2 (B).

The geometrical factor  $B$  in Equation 3.9 determines the spatial spreading geometry, and thus the spread backside area. Therefore,  $R_{Back}$  depends on the term  $B$ , and ultimately, the selected  $R_{Spread}$  model. A spreading geometry was suggested by Folchert and Brendel, which is a slightly modified version of the spreading geometry proposed by Rijnbach et al. [59]. In this thesis, both spreading geometries were employed to calculate and compare  $\rho_c$ .

When Equations 3.8 and 3.10 are taken into consideration, Equation 3.7 can be rewritten (by replacing  $R_0$  with  $R_{Back}$ ) as

$$R_T - R_{Spread} = \rho_c \left( \frac{1}{\text{front circular area}} + \frac{1}{\text{spread backside area}} \right) \quad (3.11)$$

The  $\rho_c$  value can be extracted from Equation 3.11.

In this thesis, the Cox-Strack method was used to obtain the  $\rho_c$  of p-type c-Si/MoO<sub>x</sub>/Ag passivating contacts for different MoO<sub>x</sub> thicknesses (between 3.5-30 nm). The dark I-V measurements were taken using a 2425-Keithley source meter.

### 3.4.3 Transfer-Length Method (TLM)

Although the Cox-Strack method is a powerful tool for obtaining  $\rho_c$ , it requires polished flat surfaces and is not suitable for use on textured surfaces. This is mainly because the textured surfaces with their complex geometries, featuring pyramids, grooves, and other irregularities, violate the assumptions made for spreading resistance models to work properly. For the textured surfaces, as is the case for symmetric AZO:H lifetime samples that are used in this study, TLM is the more proper way of extracting  $\rho_c$ .

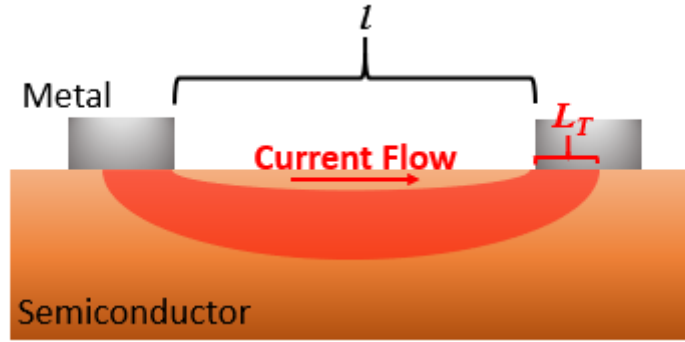


Figure 3.3. A schematic showing the current flow path and  $L_T$  during a TLM measurement

TLM uses samples with front rectangular metal bars. The total resistance  $R_T$  is measured between varying distances, such as the first and second metal bars, the first and third, the first and fourth, and so on. The path of the current passing from one metal pad to another is depicted in Figure 3.3A. The  $R_T$  measured for this path can be shown as

$$R_T = 2R_c + R_{Sheet} \frac{l}{W} \quad (3.12)$$

Where  $R_c$  is the contact resistance,  $l$  is the distance between metal pads, and  $W$  is the width of the metal pad surface that is perpendicular to the current flow direction. Similar to Equation 3.7, the resistance applied by the metal bulk is omitted in Equation 3.12 due to being significantly smaller than the other terms.

After measuring  $R_T$  values for different distances  $l$ , the slope of the linear fit of the  $R_T$  vs  $l$  graph will give the  $R_{Sheet}$ , and the residual resistance at  $l = 0$  will be equal to two times  $R_c$ . However, the  $\rho_c$  value cannot be extracted by simply multiplying the metal bar area by  $R_T$ . That is because most of the current will be sent and collected from a small area next to the edges of the metal bars, as shown in Figure 3.3A. The length of this area is called the transmission length,  $L_T$ , and it is equal to

$$L_T = \sqrt{\frac{\rho_c}{R_{Sheet}}} \quad (3.13)$$

Therefore, the effective metal bar area will be equal to  $L_T$  multiplied by  $W$ , which leads to

$$R_c = \frac{\rho_c}{L_T W} = \frac{\sqrt{R_{Sheet} \rho_c}}{W} \quad (3.14)$$

After extracting the  $R_{Sheet}$  and  $R_c$  from the  $R_T$  vs  $l$  graph, the  $\rho_c$  can be calculated from Equation 3.14.

The AZO:H on n-type TOPCon samples were used for the TLM measurements with Ag metal contact bars deposited on one surface by screen printing. PV-Tools TLM-SCAN was used for the measurements.

### 3.5 Scanning Electron Microscopy (SEM)

SEM creates high-resolution images of the sample surface by using a focused beam of high-energy electrons to scan the surface. The sample chamber is kept under high vacuum to prevent the electron beam from being scattered by molecules in the air.

In this thesis, SEM was employed only for imaging the surface morphology and topography, predominantly by the detection of secondary electrons. These electrons are low-energy electrons (less than 50 eV), which are generally released from the uppermost few nanometers due to inelastic interactions with the sent electron beam. Due to their shallow origin, secondary electrons are quite sensitive to the surface

topography, which enables SEM to create extremely high-magnification images that reveal grain size, roughness, and surface texture. In this thesis, QUANTA 400F Field Emission SEM was used to investigate the cross-section and top-down view of different AZO:H layers deposited on 200 nm thick SiO<sub>x</sub>.



## CHAPTER 4

### FABRICATION AND EXPERIMENTAL FLOW

In this chapter of the thesis, the fabrication steps of the TOPCon samples employing AZO:H and PERC samples employing MoO<sub>x</sub> passivating contacts will be explained. Additionally, the experimental flow and the deposition methods for each structure will be discussed.

#### 4.1 Fabrication and Experimental Flow of AZO:H Passivation Contacts

##### 4.1.1 ALD Process

The AZO:H layers and the capping AlO<sub>x</sub> layers in this thesis were deposited by a spatial-ALD tool. ALD is a self-limiting vapor-phase deposition method, heavily used for depositing various thin films because of their superior thickness control, uniformity, and capability to deposit high-quality layers at relatively low temperatures (commonly below 250°C). During the ALD process, a thin film is deposited by exposing the surface to alternating cycles of different gaseous species. Every cycle corresponds to a submonolayer of the material being deposited. Typically, a cycle can be separated into four stages.

1. Sending a precursor to the surface, where the precursor molecules (generally in the form of a metal center surrounded by ligands) adsorb to the surface and react with the suitable surface sites.
2. The first purging, where the excess precursor and the products arising from the prior reaction are vacuumed away.
3. Sending the co-reactant to the surface, where the co-reactant molecules adsorb to the surface and react with the ligands of the adsorbed precursor molecules

4. The second purging, where the excess co-reactant and the products arising from the prior reaction are vacuumed away.

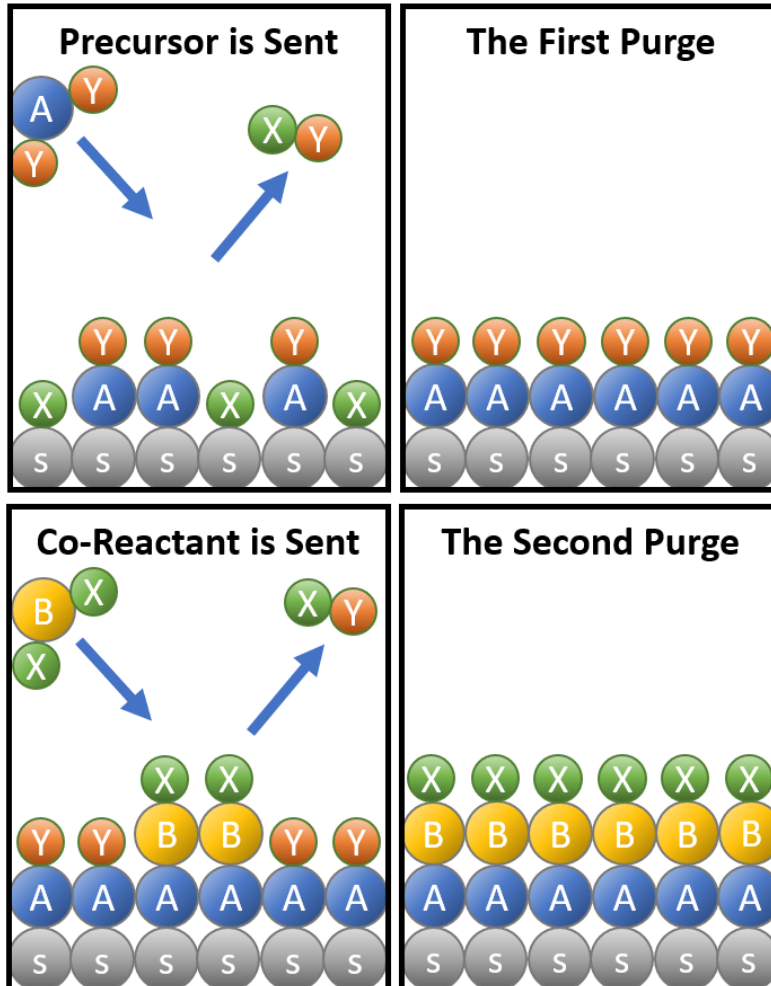
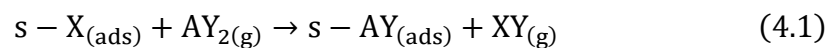
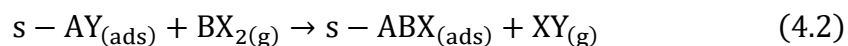


Figure 4.1. A schematic representation of the deposition steps of an ALD process

These precursors and co-reactants can, strictly, only react with either the surface or each other. Neither can react with themselves or the surface group they create, preventing the adsorption of co-reactant molecules on co-reactant molecules, or precursor molecules on precursor molecules. The nature of the alternating growth of monolayers is key to achieving self-limiting uniform deposition [60]. The stages are schematically shown in Figure 4.1, considering a binary material AB (like ZnO). The reaction that takes place in the first frame while sending the precursor is



Where  $s$  is the sample surface with adsorbed  $X$  ligand and  $AY_2$  is the precursor molecule. In the second frame, the excess molecules are purged after enough time is passed for saturation to occur (no more sites without adsorbed  $AY$ ). These two steps correspond to what is called one half-cycle. In the third frame, the co-reactant  $BX_2$  is sent as



Then, again, the excess molecules are purged after the surface saturation is reached. This repeated process gives the desired ABAB deposition on the sample surface.

The separation of the precursor and the co-reactant is vital for the ALD process to ensure cycle-by-cycle deposition. The precursor and co-reactant can be separated either by time or space. Depending on this mechanism, the ALD tool is either classified as a temporal-ALD or a spatial-ALD, respectively.

During a temporal-ALD process, the samples are placed inside a vacuum furnace. First, the furnace is filled with the precursor, and after some time, the furnace is purged. Then, the same half-cycle is repeated using the co-reactant instead of the precursor. Therefore, the temporal-ALD is a relatively slow process by its nature since there will be a pause between every step to ensure saturation and purge.

On the other hand, during a spatial-ALD process, both the precursor and the co-reactant are sent simultaneously, separated spatially by  $N_2$  gas curtains. In this design, the sample moves back and forth underneath the gas beams. There is a tiny gap between the sample and the beams. As shown in Figure 4.2, each gas outlet is placed between exhausts so the gas will interact with the surface and be purged right after. This design is much faster than the temporal-ALD design, since there is no delay between each step. In this thesis, a spatial-ALD by SALD was used for depositing AZO:H and the capping layer  $AlO_x$ .

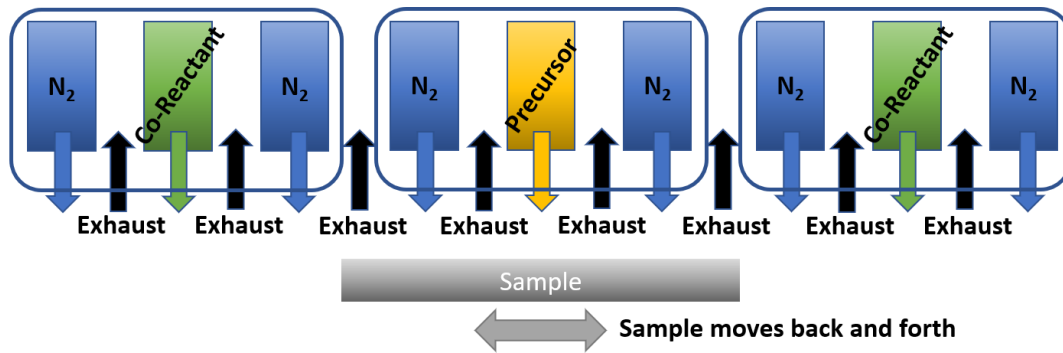


Figure 4.2. Schematic representation of the separation of precursor and co-reactant in spatial-ALD

In addition to these two half-cycle deposition, there can be used more advanced multi-step process to deposit thin films consisting of more than two types of elements, such as AZO:H. Commonly, AZO:H layers are deposited either by co-injection or supercycles.

- During a supercycle deposition, the first full cycle takes place using the ZnO precursor, and then another full cycle takes place using the  $\text{AlO}_x$  precursor for Al doping. Since the number of Al in AZO:H is desired to be much less than the number of Zn, one  $\text{AlO}_x$  cycle is sent between every  $n$  cycles of ZnO, depending on the desired Al doping ratio.
- During a co-injection deposition, both precursors for ZnO and  $\text{AlO}_x$  are sent together as a mixture. The Al doping ratio in this case is determined by varying the  $\text{AlO}_x$  precursor flow ratio to that of the ZnO precursor.

In this thesis, the co-injection method was used during the AZO:H deposition. The precursors DEZ (ZnO precursor) and DMAI (Al doping precursor) were mixed in one precursor outlet and sent together with varying ratios to test the effect of different Al doping concentrations.

### 4.1.2 Experimental Flow

AZO:H layers and  $\text{AlO}_x$  capping layers were deposited using a spatial-ALD tool. For the AZO:H deposition, DEZ and DMAI were co-injected simultaneously with the  $\text{H}_2\text{O}$  co-reactant. DMAI was chosen over TMA as the doping precursor due to its superior doping efficiency [61]. DMAI was also used for the deposition of  $\text{AlO}_x$  capping layers for convenience. Different AZO:H deposition recipes were used, varying the deposition temperature (110, 200, and 230°C), DMAI flow for Al doping (0.5 and 1.5 slm), and  $\text{H}_2\text{O}$  co-reactant flow (40 and 550 mg/min) while keeping the DEZ flow fixed at 2.0 slm. The  $\text{AlO}_x$  capping layer recipe was kept fixed with 1.5 slm DMAI and 280 mg/min  $\text{H}_2\text{O}$  flow rates; however, the deposition temperatures were changed so that both AZO:H and  $\text{AlO}_x$  deposition temperatures would match for each sample.

For the lifetime measurements, symmetrical n-TOPCon test samples were fabricated on 170 $\mu\text{m}$  p-type textured Czochralski (Cz) c-Si wafers with 0.9  $\Omega\text{cm}$  base resistivity. Around 1.1 nm tunneling thermal  $\text{SiO}_x$  and 110 nm poly Si layer were in-situ grown in a low-pressure chemical vapor deposition (LPCVD) device. Later, the n-doping on the poly-Si was realized using an atmospheric doping furnace with a phosphoryl chloride ( $\text{POCl}_3$ ) precursor.

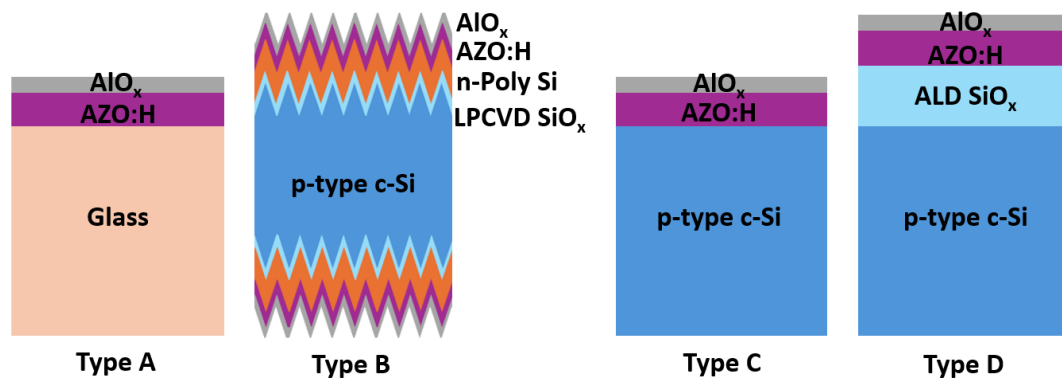


Figure 4.3. 2D schematics of the fabricated samples

AZO:H( $\text{AlO}_x$ ) layers were deposited on four different types of structures, schematically shown in Figure 4.3. For the Type A samples, 20, 88, and 200 nm thick layers were deposited with and without an  $\text{AlO}_x$  capping layer. These samples were used for transmission and four-point-probe measurements. For the Type B samples, 22 nm AZO:H layers were symmetrically deposited on the symmetric TOPCon test samples, and then the samples were cut into  $5 \times 5 \text{ cm}^2$  pieces, and each piece experienced a 5-minute annealing under forming gas at different temperatures in the  $375\text{-}525^\circ\text{C}$  range. Afterwards, low-temperature Ag contacts were deposited by screen printing for TLM measurements. Type C samples consist of AZO:H( $\text{AlO}_x$ ) deposited on  $2.5 \text{ }\Omega\text{cm}$   $280 \text{ }\mu\text{m}$ -thick double-side polished n-type FZ wafers for the ellipsometry measurements. Type D structures consist of 200 nm thick  $\text{SiO}_x$  on one side of  $2 \text{ }\Omega\text{cm}$   $280 \text{ }\mu\text{m}$ -thick Cz c-Si wafers deposited by spatial-ALD using bis(diethylamino)silane (BDEAS) as the precursor for SEM imaging. Thick  $\text{SiO}_x$  enhances the visibility of AZO:H cross-section during the SEM imaging.

Unfortunately, it was not possible to test the AZO:H passivation contacts on a finished operational TOPCon solar cell in this thesis. Instead, the  $iV_{oc}$  values and the resistive properties were analyzed to evaluate the potential usage of AZO:H layer as a passivating contact.

## **4.2 Fabrication and Experimental Flow of $\text{MoO}_x$ Passivating Contacts**

### **4.2.1 Physical Vapor Deposition (PVD)**

PVD is a broad category of vacuum deposition methods that are employed to deposit thin films on a substrate. The PVD process can be described in three steps.

1. The generation of vapor phase from a solid source material.
2. The transportation of the vapor from the source to the substrate.
3. The condensation of the vapor onto the substrate surface, where it forms the thin film.

The process is solely physical; that is, there is no chemical reaction occurring at the substrate surface. It takes place in a vacuum chamber so that the vapor won't interact with or be scattered by the atmospheric impurities. Common PVD methods include thermal and E-beam evaporation and sputtering, each of which differs in the method of vaporizing the source.

The thermal PVD method employs resistive heating to vaporize the source material. The source materials are placed in metal boats, and the chamber is vacuumed. Then the boats carrying the source materials are heated by passing a high electrical current through them. This heat leads the source materials to sublime or evaporate. The vapor travels in all directions from the source, while the sample is placed on top of the source to efficiently collect the vapor particles. The vapor, then, condenses on the cooler substrate surface. The substrate holder rotates during the process to increase the uniformity of the deposition. Meanwhile, the deposition thickness is being measured by the thickness monitor to realize accurate thickness control. This method is advantageous for its relative simplicity and high deposition rates.

In this study, the stoichiometric MoO<sub>3</sub> powder with >3N purity and Ag pellets with 99.99% purity were used as the source material. MoO<sub>x</sub> was deposited with a deposition rate of 0.6 Å/s, and Ag was deposited with 1 Å/s initially, gradually increasing to 3 Å/s. All the depositions were realized under high vacuum with chamber pressure levels around 10<sup>-5</sup> Torr. Leybold Univex 450 was used as the PVD tool.

#### **4.2.2 Experimental Flow**

The PERC solar cells with MoO<sub>x</sub> local back contact were produced using 170 μm 150 × 150 mm<sup>2</sup> Cz p-type wafers, using the common processing sequence of industrial PERC solar cells while using industrial precursors and tools. The process flow of these solar cells is displayed in Figure 4.4.

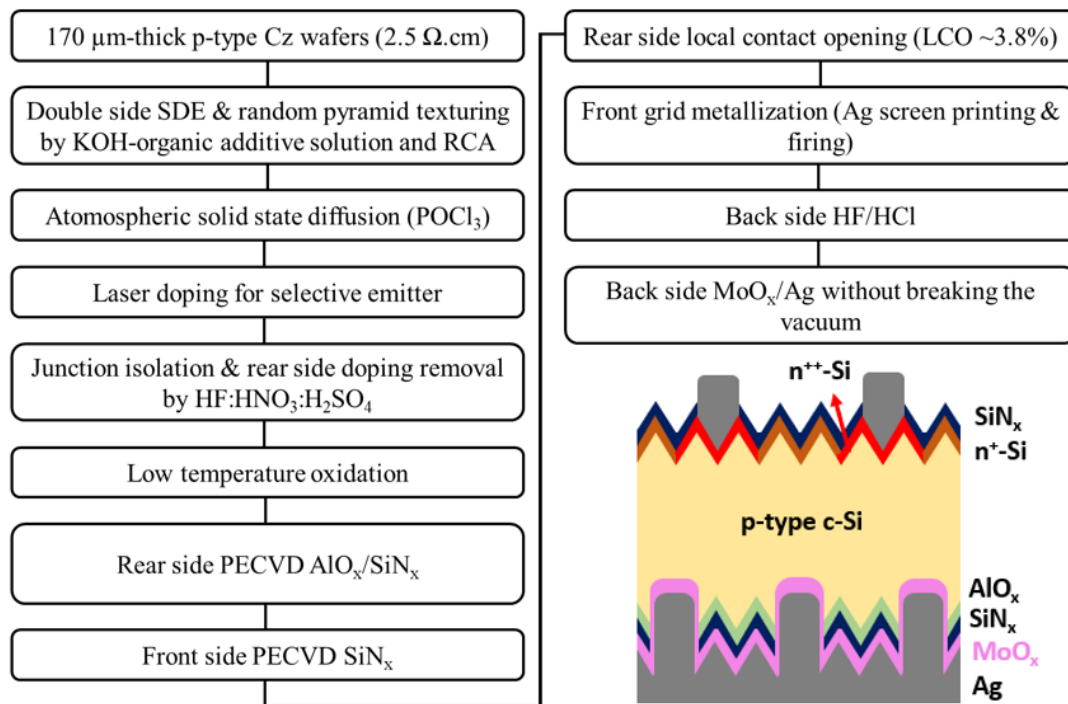


Figure 4.4. Process flow diagram of the fabrication of PERC cells employing local MoO<sub>x</sub>/Ag back contact, also showing a schematic of the final cell [56]

The wafers were first saw damage etched and pyramid textured double-side by KOH-organic additive solution, then, they were cleaned using the RCA process. The front side was n-type doped in an atmospheric furnace using POCl<sub>3</sub> precursor, and local selective emitters (n<sup>+</sup>) were formed by a laser. The rear side doping removal and the junction isolation were carried out by chemical etching in HF:HNO<sub>3</sub>:H<sub>2</sub>SO<sub>4</sub> mixture. Wafers were then passivated double-side with a thin thermal oxide. AlO<sub>x</sub>/SiN<sub>x</sub> stacks were applied on the back side using a PECVD tool, and only SiN<sub>x</sub> was applied on the front as an ARC, again, by PECVD. The back surface AlO<sub>x</sub>/SiN<sub>x</sub> stack was laser processed to form local contact openings (LCO) on approximately 3.8% of the whole surface area. Later, the front side metal contacts were deposited in the form of five Ag busbars and Ag fingers by utilizing screen printing and firing. Then the back side was cleaned with an HF/HCl mixture right after the wafers were put into the PVD vacuum chamber to prevent oxidation. Using thermal PVD, 3.5, 5, 7, 15, and 30 nm of MoO<sub>x</sub> with 300 nm Ag layers were deposited without breaking the vacuum. These

solar cells were characterized by I-V measurements under a solar simulator under standard 1-sun conditions (1000 kW/m<sup>2</sup>, AM 1.5 spectrum).

Double-sided MoO<sub>x</sub> with the same set of thicknesses was also deposited on 250 μm thick double-side polished p-type FZ c-Si wafers with 1 Ωcm base resistivity for SE and QSSPC measurements. The Cox-Strack test structures were also fabricated using the same wafer substrates in the structure design explained in Figure 3.2. During the deposition of the MoO<sub>x</sub>/Ag stack onto the front surface, a mask with circular openings with different diameters (3.5-1.3 mm) was used.



## CHAPTER 5

### RESULTS AND DISCUSSION

In this chapter, the characterization results of the AZO:H and MoO<sub>x</sub> passivating contacts are presented and discussed.

#### 5.1 Results for AZO:H

##### 5.1.1 AZO:H on TOPCon

The AZO:H(/AlO<sub>x</sub>) layers were deposited on symmetric n-TOPCon samples for the evaluation of the passivation quality of AZO:H(/AlO<sub>x</sub>) on n-type poly-Si layers, which are the standard type of poly-Si layers used in the industrial TOPCon solar cells. The deposition parameters of these layers for symmetric lifetime samples, along with their thicknesses measured by SE, are given in Table 5.1. The DMAI flow rate is kept fixed at 1.5 slm for this set of depositions.

Table 5.1 Deposition parameters of AZO:H layers on symmetric lifetime samples with corresponding thickness measured by SE

Deposition Temperature (°C)	H <sub>2</sub> O Flow (mg/min)	AlO <sub>x</sub> Capping Thickness (nm)	AZO Thickness (nm)
230	550	0	19.5
230	550	19.3	17.3
230	40	0	20.3
230	40	19.4	17.1
200	40	20.4	24.4
110	40	0	22.1
110	40	19.2	24.2

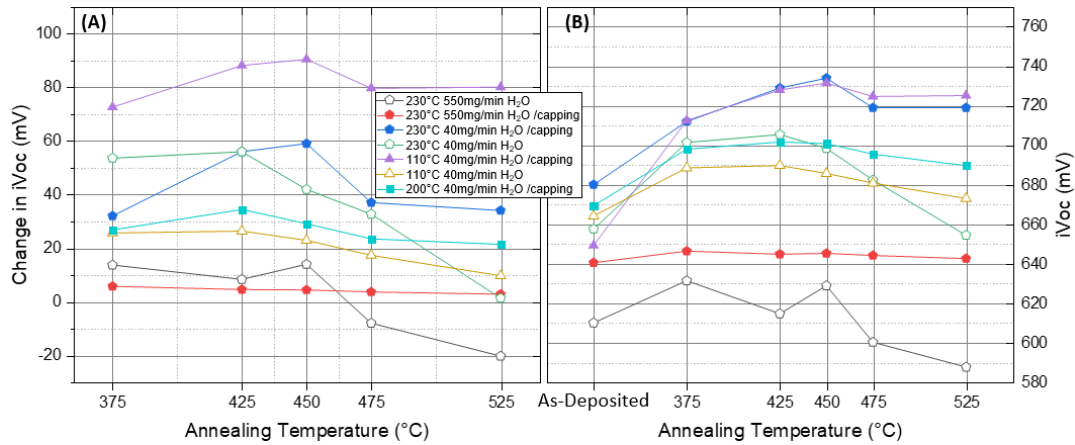


Figure 5.1. (A) Change in  $iV_{oc}$  and (B)  $iV_{oc}$  values of the AZO:H(/AlO<sub>x</sub>) stacks deposited on symmetric n-TOPCon samples for different forming gas annealing temperatures

The change in  $iV_{oc}$  values and the resulting  $iV_{oc}$  of the symmetrical n-TOPCon samples are given in Figure 5.1. TOPCon/AZO:H samples with AlO<sub>x</sub> resulted in excellent passivation quality, peaking at 450 °C, with impressive  $iV_{oc}$  values reaching 734 mV with a  $J_0$  of 6.5 fA/cm<sup>2</sup> per side, demonstrating the outstanding capability of AZO:H/AlO<sub>x</sub> stacks as an excellent hydrogen source. While their uncapped counterparts were still able to improve the passivation by up to 56 mV at 425°C, they resulted in lower  $iV_{oc}$  values.

In addition, uncapped samples showed lower thermal stability. At temperatures higher than 425°C, the passivation level of uncapped samples started decreasing, likely due to hydrogen effusion from uncapped AZO:H during annealing. This decrease is less evident for the samples with capping, especially at 525°C, since the capping layer partially prevents the effusion. The AZO:H deposited at 110°C outperformed the one deposited at 200°C and resulted in the largest improvement by about 90 mV after annealing at 450°C, and resulted in similar  $iV_{oc}$  values as high as the one deposited at 230°C.

The behavioral difference between capped and uncapped AZO:H under annealing is a strong clue that the main passivation mechanism of AZO:H is hydrogenation. The AlO<sub>x</sub> capping prevents the hydrogen from effusing out of the sample, as suggested

by [17]. Instead, in the capped samples, the hydrogen in AZO:H diffuses through the poly-Si and to the c-Si/SiO<sub>x</sub> interface. Hydrogenating the interface and healing D<sub>it</sub>.

The comparison of the uncapped versions of AZO:H deposited at 110 and 230°C shows that the 230°C one outperforms by >10 mV at lower annealing temperatures. Since in the uncapped case, the hydrogen effusion limits the  $iV_{oc}$ , this behavior might be a result of the different crystalline quality, due to their different deposition temperature, dictating the hydrogen effusion rate.

The samples deposited with a 550 mg/min H<sub>2</sub>O flow show very low enhancement in passivation. Increasing the H<sub>2</sub>O flow to very high levels during deposition might have resulted in insufficient purging of the co-reactant and molecular H<sub>2</sub>O being physisorbed into the AZO:H layer, creating local defects.

Since the samples with capping result in higher hydrogenation during FGA, the hydrogen in AZO:H might be introduced by the co-reactant H<sub>2</sub>O during the deposition, instead of the forming gas during FGA. In order to test this hypothesis, an unannealed 5×5 cm<sup>2</sup> piece of the AZO:H/AlO<sub>x</sub> deposited at 230°C with 40 mg/min was annealed at 450°C for 5 minutes under N<sub>2</sub> environment, instead of forming gas. The resulting  $iV_{oc}$  and  $J_0$  values were 728 mV and 7.5 fA/cm<sup>2</sup> per side. The closeness of these results to those of the one annealed under the forming gas ambient shows that the AZO:H/AlO<sub>x</sub> stacks were already hydrogenated prior to the FGA process, and the ultra-high passivation by AZO:H/AlO<sub>x</sub> stacks is achievable even with N<sub>2</sub> annealing, which is a more common process than FGA in industry.

### 5.1.2 Optical Properties

The transmission results for AZO:H with 20 nm (both with and without a capping layer), 88 nm, and 200 nm, along with bare glass substrate transmission, are given in Figure 5.2. These AZO:H layers were deposited with 40 mg/min H<sub>2</sub>O flow and 1.5 slm DMAI flow. AZO:H on glass substrate demonstrates excellent transparency with all 20, 88, and 200 nm AZO:H, resulting in more than 80% between 380-1200 nm

wavelengths, while 20 nm AZO:H predominantly maintains a transmission level of around 90%. The 88 nm AZO:H gives lower transmission than 200 nm in the wavelength range 550-900 nm, but still remains between 80-90% range between 380-1200 nm wavelengths. The non-etched capping layer decreases the transmission level by only 1-2% in the visible range.

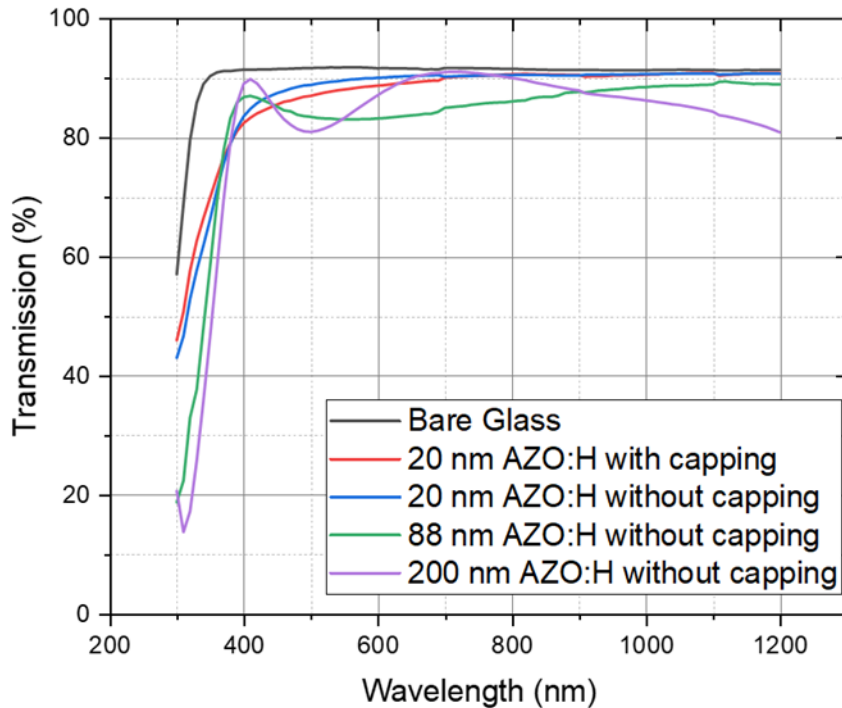


Figure 5.2. Transmission results for bare glass substrate, 20 nm AZO:H(/AlO<sub>x</sub>), 88 nm, and 200 nm AZO:H

In Figure 5.3, the transmission results of the samples with different deposition parameters were compared for 20 nm AZO:H without capping. The samples deposited at 110°C showed slightly higher transmission than 200 and 230°C, reaching 90% transmission at 550 nm wavelength. For 20 nm samples deposited at 230°C, H<sub>2</sub>O co-reactant flow showed no significant effect on transparency; on the other hand, a higher doping rate gave slightly higher transmission at wavelengths below 600 nm. This slight increase in transmission in the lower wavelengths might be due to the increase in  $E_g$  caused by higher Al doping following the Burstein-Moss effect.

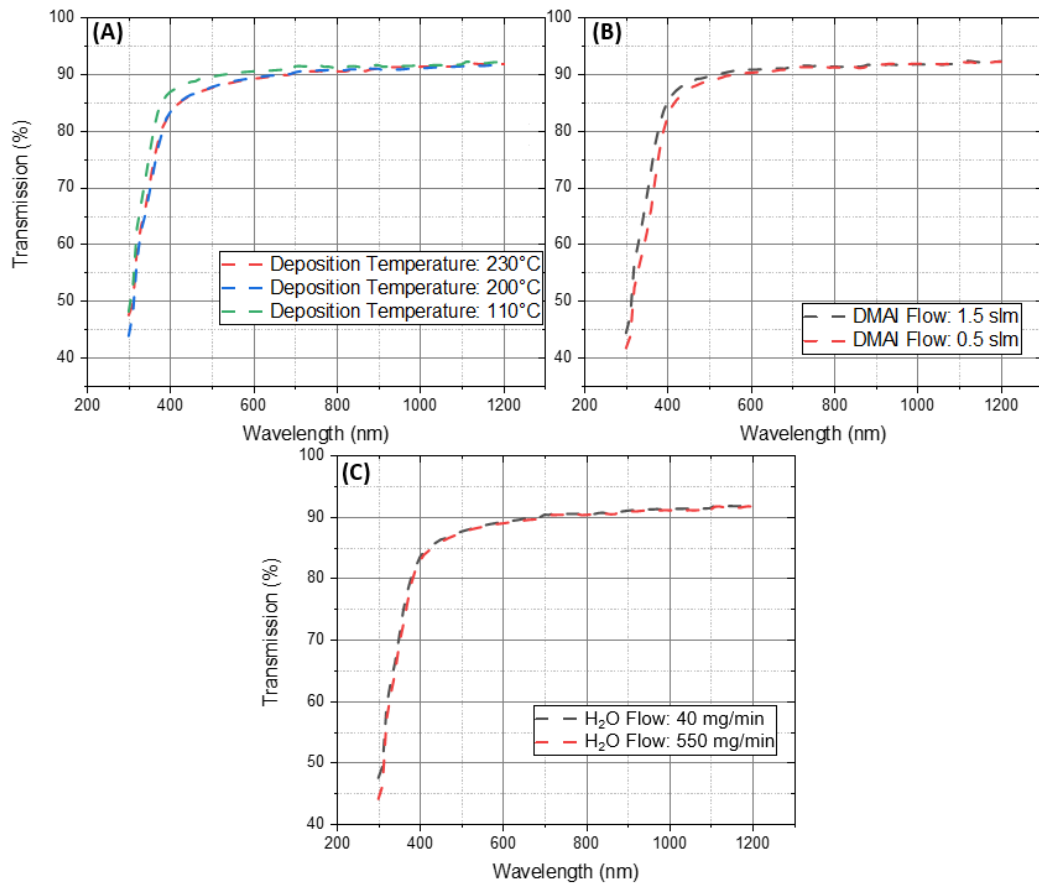


Figure 5.3. Transmission results for varying (A) deposition temperature, (B) DMAI flow, and (C) H<sub>2</sub>O Flow

These exceptionally high transmission results show that AZO:H layers can be successfully used at the back side of bifacial TOPCon solar cells since AZO:H will not result in optical losses.

### 5.1.3 Structural Properties

Figure 5.4 presents the top-down SEM images of 200 nm and 80 nm AZO:H layers deposited at 230°C. There is a clear enlargement in grain size of the AZO:H as the thickness is increased. As the thickness increases, crystals start merging into each other and resulting in an improved crystallinity.

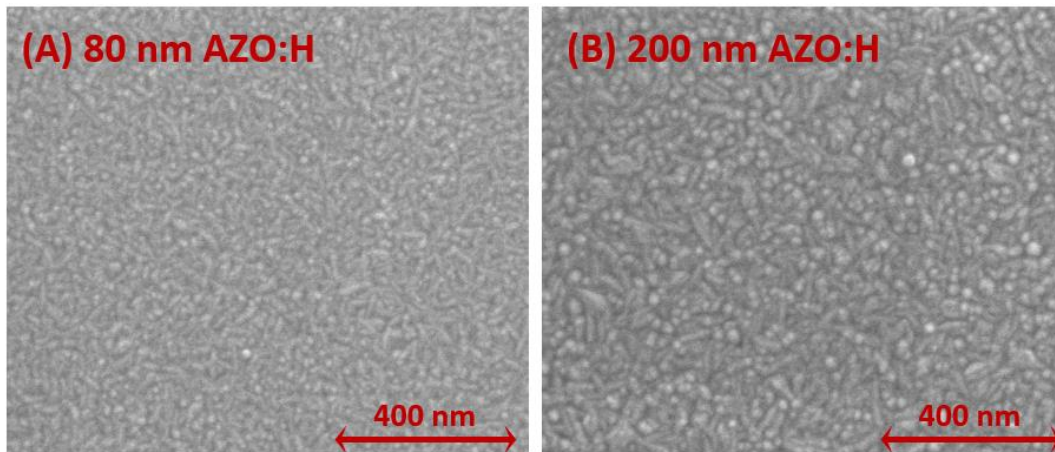


Figure 5.4. SEM images of (A) 80 nm and (B) 200 nm AZO:H

Figure 5.5 shows the cross-sectional SEM image of 200 nm AZO:H deposited on 200 nm SiO<sub>x</sub>. The ALD-deposited AZO:H shows directional poly-crystalline growth perpendicular to the sample surface. This characteristic vertical crystal structure of AZO:H favors vertical conductivity, especially at low thicknesses where the grain sizes are smaller, as shown in the next section.

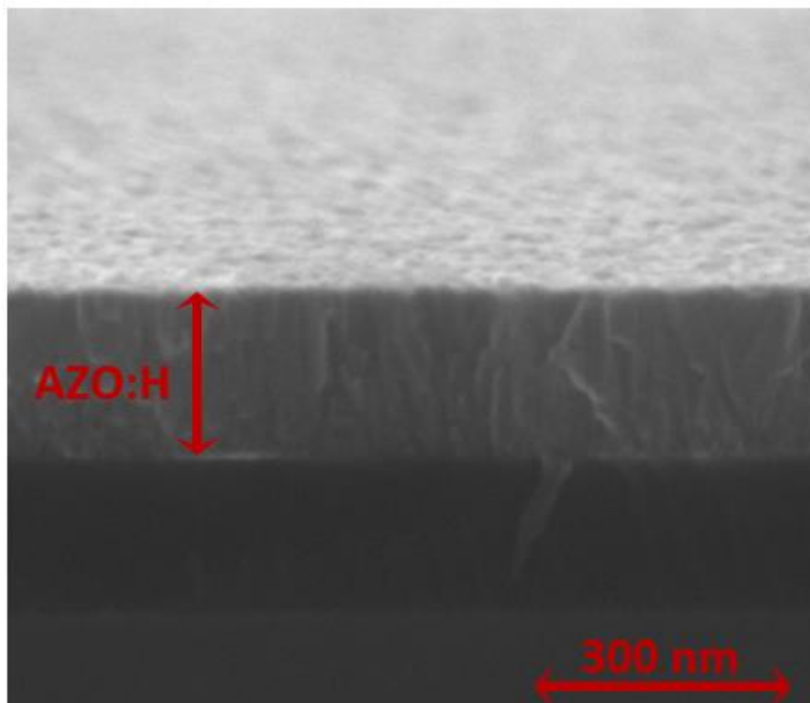


Figure 5.5. Cross-sectional SEM image of 200 nm AZO:H on 200 nm SiO<sub>x</sub>

#### 5.1.4 Electrical Properties

The  $R_{Sheet}$  values obtained by four-point-probe measurements on the glass samples (type A) for different parameters are shown in Figure 5.6. In Figure 5.6A, 20 nm AZO:H layers deposited at 230°C are compared depending on their DMAI flow and H<sub>2</sub>O co-reactant flow during deposition. It is shown that increasing the DMAI flow reduces the sheet resistance by more than 1 MΩ/sq. The higher DMAI flow introduces more Al doping in ZnO and results in increased carrier density due to interstitial Al acting as an electron donor in the ZnO matrix. On the other hand, increasing the co-reactant H<sub>2</sub>O flow from 40 to 550 mg/min leads to higher  $R_{Sheet}$ . These results support the idea of the excess amount of H<sub>2</sub>O flow causing H<sub>2</sub>O to be physisorbed into the AZO:H layer or excess hydrogen and oxygen forming defects inside the AZO:H, which, alongside causing reduced passivation, also results in less conductive layers.

Figure 5.6B compares different AZO:H thicknesses deposited at different temperatures with deposition parameters of 40 mg/min H<sub>2</sub>O flow and 1.5 slm DMAI flow. The  $R_{Sheet}$  of AZO:H layer is highly dependent on the thickness since its grain size increases with increased thickness of the layer, as shown in the previous section. For the AZO:H deposited at 230°C, the  $R_{Sheet}$  decreases from 343 kΩ/sq at 20 nm to about 1000 Ω/sq at 80 nm and below 100 Ω/sq at 200 nm thickness. In addition, the increased deposition temperature also showed reduced  $R_{Sheet}$  due to improved crystallinity.

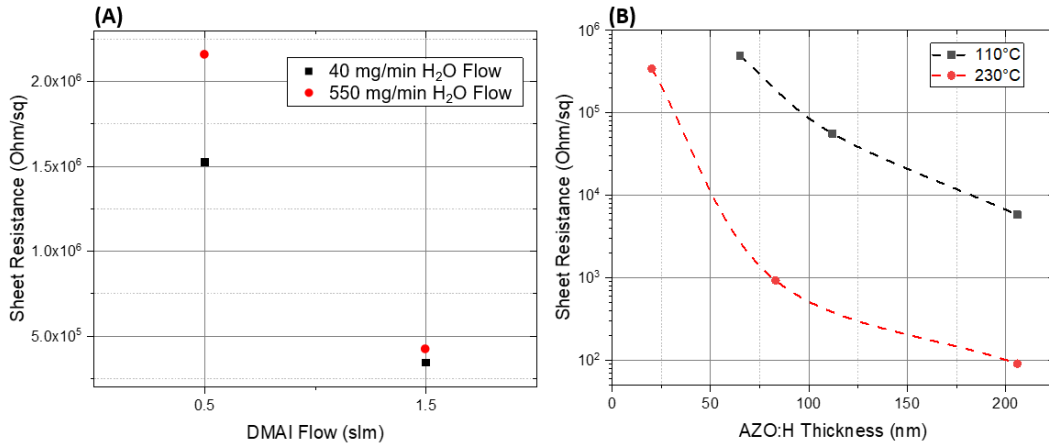


Figure 5.6.  $R_{Sheet}$  results (A) for different DMAI and H<sub>2</sub>O flows for 20 nm AZO:H deposited at 230°C, and (B) for different thicknesses deposited at 110 and 230°C

For the measurement of  $\rho_c$  values of 20 nm AZO:H on n-type poly-Si, Ag metal bars were deposited on one surface of the Type B symmetric lifetime test samples to be used for TLM measurements. In order for TLM measurements to be valid on a multi-layer stack, the lateral conduction must occur through one layer only [62]. This can be realized due to 20 nm AZO:H favoring vertical conductivity over lateral conductivity, and its  $R_{Sheet}$  values being over 1000 times higher than the n-type poly-Si. Regardless, the  $R_{Sheet}$  of n-TOPCon on p-type c-Si was measured by a four-point probe to compare it with the  $R_{Sheet}$  measured at TLM. The four-point probe resulted in  $208 \pm 10 \Omega/\text{sq}$ , which falls in the same range of  $R_{Sheet}$  values measured by the TLM shown in Figure 5.7A, indicating that the lateral current transport dominantly occurs through the n-type poly-Si layer.

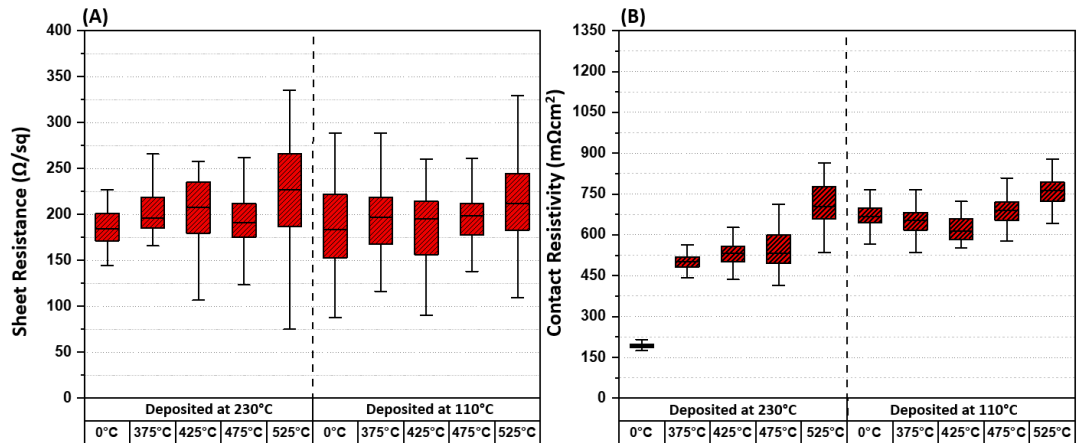


Figure 5.7. (A)  $R_{Sheet}$  and (B)  $\rho_c$  values measured by TLM for 20 nm AZO:H deposited and forming gas annealed at different temperatures

Figure 5.7B shows the  $\rho_c$  results for 20 nm AZO:H deposited at 230 and 110°C, later annealed under forming gas for different temperatures without an AlO<sub>x</sub> capping layer. The  $\rho_c$  of AZO:H deposited at 230°C is around 175 mΩcm<sup>2</sup> in the as-deposited case, and it increases to 475-575 mΩcm<sup>2</sup> range for annealing temperatures below 525°C. The increase in resistivity after annealing of AZO:H without a capping layer is commonly observed [21,35], and caused by hydrogen effusion and the reactions with the ambient gas. The relatively steep increase at 525°C might be further induced by the AZO:H/poly-Si interface starting to get roughened, as is the case with AZO/SiO<sub>x</sub>/c-Si [21]. The AZO:H layer deposited at 110°C shows much higher  $\rho_c$  in the as-deposited case relative to one deposited at 230°C. This behavior is similar to the  $R_{Sheet}$  results and is likely due to the worse crystallization of the layer at lower deposition temperatures. The initial decrease in  $\rho_c$  until the annealing temperature of 425°C further supports this idea and shows that the behavior of  $\rho_c$  is determined dominantly by the improvement of the crystallinity instead of hydrogen effusion and ambient gas effects at these temperatures. Nevertheless, the  $\rho_c$  starts increasing again after FGA at 475°C.

These results show that thin (below 20 nm) AZO:H indeed favors vertical conductivity over lateral conductivity due to its directional crystal growth direction. Although the  $\rho_c$  is much larger than the state-of-the-art passivating contact schemes,

it was shown that the  $\rho_c$  of the AZO:H can be significantly reduced by two orders of magnitude by reducing the AZO:H thickness to 10 nm from 18 nm and depositing a thin LiF layer in between the metal contact and AZO:H without losing significant passivation [38]. Although this will further increase the  $R_{Sheet}$ , depositing AZO:H on n-type poly-Si with high lateral conductivity eliminates the requirement for good lateral conductivity for AZO:H, since the lateral transport of the charge carriers will occur mainly through the poly-Si layer. Overall, a thin AZO:H layer can be used as a hydrogen-rich passivation layer at the rear side of the mono-facial TOPCon solar cells between the poly-Si and metal.

Another promising potential application of AZO:H on n-type poly-Si is being employed as a recombination junction in TOPCon-like bottom cell/perovskite top cell tandem structures. The excellent transparency and passivating quality of AZO:H ensure the effective photon collection and high passivation at the bottom cell. In addition, its high  $R_{Sheet}$  values can increase the overall performance by limiting the shunting effect of the top cell, which is a common problem with large-area perovskites [63].

## 5.2 Results for MoO<sub>x</sub>

### 5.2.1 Electrical Properties

A variety of Cox-Strack test samples with varying MoO<sub>x</sub> thicknesses were prepared in order to observe the behavior of  $\rho_c$  depending on thickness. Figure 5.8A shows the non-Ohmic characteristic of the dark I-V results of the direct c-Si/Ag stack without a MoO<sub>x</sub> layer in between. Each line in Figure 5.8A and B represents a measurement taken with the probe making contact on a different front circular pad with varying diameters. Unlike the direct c-Si/Ag case, the dark I-V measurements resulted in a desired linear behavior for all the tested c-Si/MoO<sub>x</sub>/Ag stacks with MoO<sub>x</sub> thicknesses of 3.5, 5, 7, 15, and 30 nm. Figure 5.8B shows the dark I-V results for the sample with 5 nm MoO<sub>x</sub>.

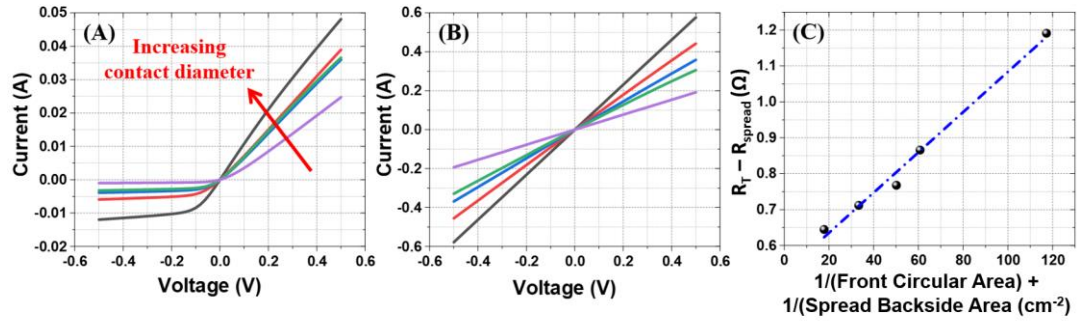


Figure 5.8. The dark I-V results for the test samples with (A) c-Si/Ag without MoO<sub>x</sub> and (B) 5 nm MoO<sub>x</sub> between c-Si and Ag. (C)  $R_T - R_{\text{spread}}$  vs  $(\text{front circular area})^{-1} + (\text{spread backside area})^{-1}$  plot for the test sample with 5 nm MoO<sub>x</sub> [56]

The  $\rho_c$  value is extracted from the slope of the linear fit shown in Figure 5.8C, following Equation 3.11. As described in Chapter 3, two different spreading models were used in the calculation of  $\rho_c$ . Both models resulted in similar values (Table 5.2), with the Folchert and Brendel model giving about 14% larger results than the Rijnbach et al.

Table 5.2 The  $\rho_c$  results for different MoO<sub>x</sub> thicknesses [56]

MoO <sub>x</sub> thickness (nm)	$\rho_c$ (Folchert and Brendel) (m $\Omega\text{cm}^2$ )	$\rho_c$ (Rijnbach et al.) (m $\Omega\text{cm}^2$ )
3.5	6.6	5.7
5	5.6	4.8
7	5.9	5.1
15	6.3	5.4
30	16.1	13.8

The 5 nm MoO<sub>x</sub> gives the lowest  $\rho_c$  values of 5.6 or 4.8 m $\Omega\text{cm}^2$ , depending on the used model. Such low levels of  $\rho_c$  indicate the efficient hole transport through p-type c-Si/MoO<sub>x</sub>/Ag passivating contact, with minimized electrical loss. The thicker the MoO<sub>x</sub> gets, its  $\rho_c$  increases. This behavior is very common for MoO<sub>x</sub> because at

increased thicknesses, the large bulk resistivity of MoO<sub>x</sub> starts dominating the total  $\rho_c$  [41]. On the other hand, the thinner 3.5 nm MoO<sub>x</sub> also resulted in an increased  $\rho_c$ , which can be explained by the insufficient, partial surface coverage of MoO<sub>x</sub> at very low thicknesses. Volmer-Weber nucleation is very common for such metal oxide thin films being deposited by thermal PVD, which means the MoO<sub>x</sub> starts growing as islands on the c-Si surface instead of full-area layers [41,43].

### 5.2.2 MoO<sub>x</sub> on PERC

The same set of thicknesses in Table 5.2 was used in the production of the complete PERC cells, utilizing local MoO<sub>x</sub>/Ag passivating contacts at the rear side. The solar cell parameters extracted from I-V measurements under the solar simulator are represented in Table 5.3.

Table 5.3 Solar cell parameters of PERC cells utilizing different thicknesses of local MoO<sub>x</sub>/Ag back contacts [56]

MoO <sub>x</sub> thickness (nm)	$V_{oc}$ (mV)	$J_{sc}$ (mA/cm <sup>2</sup> )	FF (%)	Efficiency (%)
3.5	650	39.3	75.38	19.25
5	672.3	39.7	80.66	21.53
7	672.4	39.9	79.50	21.33
15	670.4	39.0	76.39	19.99
30	652.3	35.8	40.20	9.38

3.5 nm MoO<sub>x</sub> gives low FF along with low  $V_{oc}$  because of the insufficient surface coverage, leading to partial direct c-Si/Ag contacts with high recombination and no passivation. The samples with 5 to 15 nm MoO<sub>x</sub> show a higher passivation quality of more than 670 mV due to their uniformity and sufficient surface coverage.

The differences in the overall efficiencies at these thicknesses are predominantly determined by the resistive losses and the corresponding FF of these solar cells. Figure 5.9 compares the  $\rho_c$  to FF values for different MoO<sub>x</sub> thicknesses.

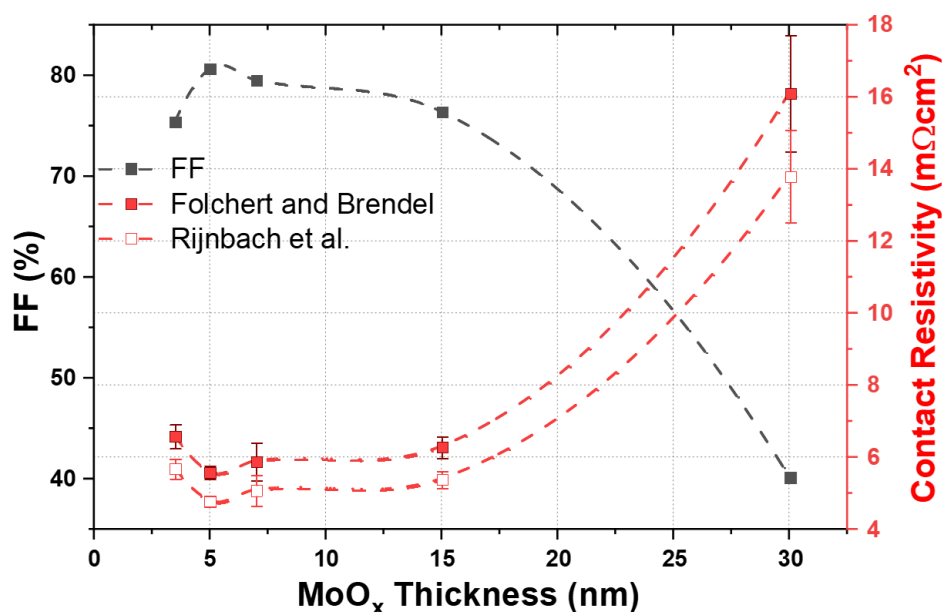


Figure 5.9. Change in FF and  $\rho_c$  with varying MoO<sub>x</sub> thickness [56]

The cell with 5 nm local MoO<sub>x</sub>/Ag contacts resulted in the best efficiency with 21.53% due to successfully minimizing the  $\rho_c$  and maximizing the  $V_{oc}$ . The low  $\rho_c$  of this design resulted in the highest FF of 80.66%. These results are quite high compared to the previous literature results on both full-area MoO<sub>x</sub> [49] and locally contacted MoO<sub>x</sub> [54]. The I-V properties under 1-sun conditions for the best-performing solar cell are shown in Figure 5.10.

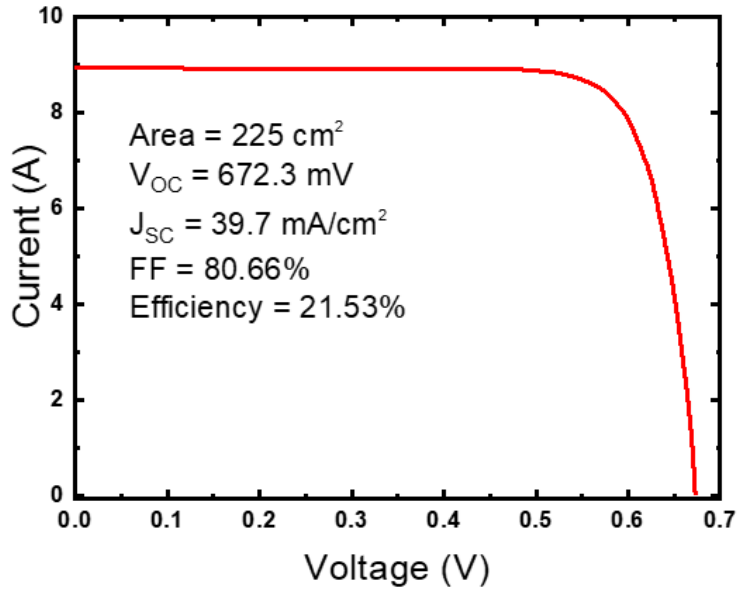


Figure 5.10. The I-V results under 1-sun for the best-performing PERC solar cell employing 5 nm local MoO<sub>x</sub>/Ag [56]

In addition, the  $J_0$  of 5 nm MoO<sub>x</sub> on p-type c-Si was measured using symmetrically deposited full-area MoO<sub>x</sub> with different thicknesses on p-type FZ c-Si. The test structure resulted in 68.5 fA/cm<sup>2</sup> per side. The  $J_0$  of MoO<sub>x</sub> stays behind the state-of-the-art designs like TOPCon or SHJ [64]. Regardless, it still shows quite superior chemical passivation, which is translated into a  $V_{oc}$  of 672.3 mV, compared to direct metal/c-Si (with moderate doping) contacts that result in  $J_0$  values of more than 10<sup>5</sup> fA/cm<sup>2</sup> [65].

The quantum efficiency measurements for the best-performing solar cell are shown in Figure 5.11, which contains EQE, IQE, and the reflection. The measurements were taken from the top surface, between the metal grids. The results are similar to a common c-Si solar cell. The 5 nm MoO<sub>x</sub> layer at the rear side is seemingly causing no significant reflection, as expected.

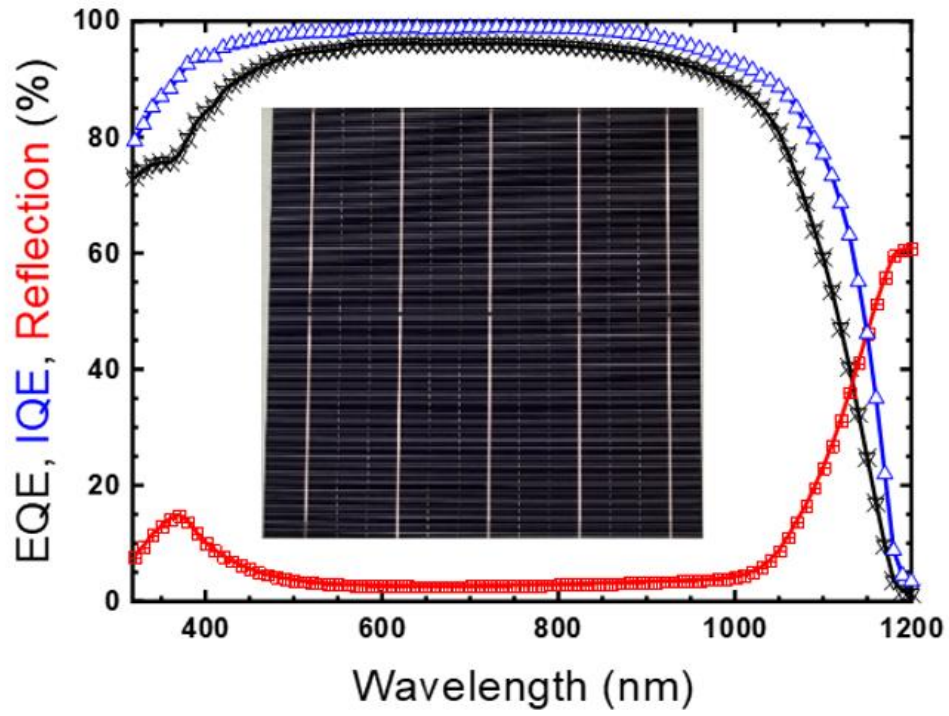


Figure 5.11. The quantum efficiency measurements for the best-performing cell with the image of the front surface of the complete solar cell [56]



## CHAPTER 6

### CONCLUSION

This thesis successfully developed and characterized two distinct metal oxide-based passivating contacts, demonstrating their significant potential for enhancing the performance of industrially relevant silicon solar cell technologies. For TOPCon applications, an electron-selective AZO:H contact was investigated. An optimized AZO:H/ $\text{AlO}_x$  stack deposited on an n-type poly-Si structure achieved an excellent  $iV_{oc}$  of 734 mV and a remarkably low  $J_0$  of 6.5 fA/cm<sup>2</sup>. A critical finding was the role of the  $\text{AlO}_x$  capping layer in retaining hydrogen within the film stack during thermal treatment, which enabled the use of a standard  $\text{N}_2$  anneal to achieve passivation levels ( $iV_{oc}$  of 728 mV and of  $J_0$  7.5 fA/cm<sup>2</sup>) comparable to a more complex forming gas anneal.

For PERC technology, a hole-selective local  $\text{MoO}_x$  back contact was integrated into an industrial fabrication sequence. By systematically varying the layer thickness, an optimal value of 5 nm was identified, which effectively balanced the trade-off between surface passivation and charge extraction. This optimization culminated in a champion large-area PERC solar cell with a power conversion efficiency of 21.53%, primarily driven by a high  $V_{oc}$  of 672.3 mV and an excellent fill factor of 80.66%.

The implications of these findings are substantial. The work on AZO:H not only demonstrates its excellent passivation potential for TOPCon cells but also highlights its multifunctionality as a transparent conductive layer, making it a candidate for bifacial cells or as a recombination junction in future tandem devices. The discovery that a simple  $\text{N}_2$  anneal is sufficient for activation significantly enhances its industrial viability by aligning with existing, low-cost manufacturing processes. The research on  $\text{MoO}_x$  provides a compelling validation of its use as a low-temperature upgrade

for the vast existing PERC manufacturing base. Achieving a higher efficiency on industrial Cz wafers than previously reported on superior FZ wafers underscores the robustness and commercial potential of the developed local contact scheme, offering a practical path to boost the performance of the current market-dominant technology.

Future research should build directly upon these promising results. For the AZO:H contact, the logical next step is the fabrication and characterization of a complete TOPCon solar cell to translate the excellent lifetime results into demonstrated device efficiency. Further investigation into reducing its contact resistivity, potentially through the use of thinner layers or the integration of interlayers like LiF as suggested in the literature, is a key avenue for optimization. For the MoO<sub>x</sub> contact, future work must focus on long-term stability and degradation studies, as thermal stability is a known concern for this material. A critical step towards commercialization would be to explore alternative capping layers or encapsulation schemes that can protect the MoO<sub>x</sub> layer during the high-temperature module lamination process, ensuring the durability of the efficiency gains demonstrated in this work.

## REFERENCES

- [1] IPCC, 2023: Climate Change 2023: Synthesis Report, Summary for Policymakers. Contribution of Working Groups I, II and III to the Sixth Assessment Report of the Intergovernmental Panel on Climate Change [Core Writing Team, H. Lee and J. Romero (eds.)]. IPCC, Geneva, Switzerland., 2023. <https://doi.org/10.59327/IPCC/AR6-9789291691647.001>.
- [2] IRENA, Renewable Power Generation Costs in 2023, Abu Dhabi, 2024.
- [3] VDMA Photovoltaics Equipment, International Technology Roadmap for Photovoltaics (ITRPV) 2023 Results, (2024).
- [4] G.C. Righini, F. Enrichi, Chapter One - Solar cells' evolution and perspectives: a short review, in: Solar Cells and Light Management: Materials, Strategies and Sustainability, Elsevier, 2020: pp. 1–32. <https://doi.org/10.1016/B978-0-08-102762-2.00001-X>.
- [5] W. Shockley, W.T. Read, Statistics of the Recombinations of Holes and Electrons, Physical Review 87 (1952) 835. <https://doi.org/10.1103/PhysRev.87.835>.
- [6] P. Procel, V. Maccaronio, F. Crupi, G. Cocorullo, M. Zanuccoli, P. Magnone, C. Fiegna, Analysis of the impact of doping levels on performance of back contact - back junction solar cells, Energy Procedia 55 (2014) 128–132. <https://doi.org/10.1016/J.EGYPRO.2014.08.095>.
- [7] W.D. Eades, Characterization of Silicon-Silicon Dioxide Interface Traps Using Deep Level Transient Spectroscopy (Surface Recombination, Semiconductor, Generation, Cross Section, Solar Cell), Stanford University, 1985.
- [8] F. Feldmann, M. Bivour, C. Reichel, M. Hermle, S.W. Glunz, Passivated rear contacts for high-efficiency n-type Si solar cells providing high

interface passivation quality and excellent transport characteristics, *Solar Energy Materials and Solar Cells* 120 (2014) 270–274.  
<https://doi.org/10.1016/J.SOLMAT.2013.09.017>.

- [9] A. Cuevas, T. Allen, J. Bullock, Y. Wan, D. Yan, X. Zhang, Skin care for healthy silicon solar cells, 2015 IEEE 42nd Photovoltaic Specialist Conference, PVSC 2015 (2015).  
<https://doi.org/10.1109/PVSC.2015.7356379>.
- [10] S.W. Glunz, B. Steinhauser, J.I. Polzin, C. Luderer, B. Gröbel, T. Niewelt, A.M.O.M. Okasha, M. Bories, H. Nagel, K. Krieg, F. Feldmann, A. Richter, M. Bivour, M. Hermle, Silicon-based passivating contacts: The TOPCon route, *Progress in Photovoltaics: Research and Applications* 31 (2023) 341–359. <https://doi.org/10.1002/PIP.3522>.
- [11] J. Bullock, C. Samundsett, A. Cuevas, D. Yan, Y. Wan, T. Allen, Proof-of-Concept p-Type Silicon Solar Cells With Molybdenum Oxide Local Rear Contacts, *IEEE J Photovolt* (2015).  
<https://doi.org/10.1109/PVSC.2015.7356165>.
- [12] G. Beaucarne, G. Agostinelli, J. Szlufcick, P. Choulat, G. Beaucarne, LOCAL CONTACT STRUCTURES FOR INDUSTRIAL PERC-TYPE SOLAR CELLS, 20th European Photovoltaic Solar Energy Conference (2005). <https://www.researchgate.net/publication/284670341> (accessed July 24, 2025).
- [13] M.A. Green, E.D. Dunlop, M. Yoshita, N. Kopidakis, K. Bothe, G. Siefer, X. Hao, J.Y. Jiang, Solar Cell Efficiency Tables (Version 66), *Progress in Photovoltaics: Research and Applications* 33 (2025) 795–810.  
<https://doi.org/10.1002/PIP.3919>.
- [14] R. Zhong, P. Padhamnath, W.J. Choi, Y.W. Ok, S. Dasgupta, A. Rohatgi, Detailed investigation of electrical and optical properties of textured n-type and roughened p-type tunnel oxide passivated contacts for screen-printed

- double-side passivated contact silicon solar cell application, *Thin Solid Films* 783 (2023) 140046. <https://doi.org/10.1016/J.TSF.2023.140046>.
- [15] A. Richter, R. Müller, J. Benick, F. Feldmann, B. Steinhauser, C. Reichel, A. Fell, M. Bivour, M. Hermle, S.W. Glunz, Design rules for high-efficiency both-sides-contacted silicon solar cells with balanced charge carrier transport and recombination losses, *Nature Energy* 2021 6:4 6 (2021) 429–438. <https://doi.org/10.1038/s41560-021-00805-w>.
- [16] J. Ding, Y. Zhou, G. Dong, M. Liu, D. Yu, F. Liu, Solution-processed ZnO as the efficient passivation and electron selective layer of silicon solar cells, *Progress in Photovoltaics: Research and Applications* 26 (2018) 974–980. <https://doi.org/10.1002/pip.3044>.
- [17] B.W.H. Van De Loo, B. Macco, J. Melskens, W. Beyer, W.M.M. Kessels, Silicon surface passivation by transparent conductive zinc oxide, *J Appl Phys* 125 (2019). <https://doi.org/10.1063/1.5054166/1074533>.
- [18] B. Sang, A. Yamada, M. Konagai, Growth of boron-doped ZnO thin films by atomic layer deposition, *Solar Energy Materials and Solar Cells* 49 (1997) 19–26. [https://doi.org/10.1016/S0927-0248\(97\)00171-2](https://doi.org/10.1016/S0927-0248(97)00171-2).
- [19] D.J. Lee, J.Y. Kwon, J. Kim, K.J. Kim, Y.H. Cho, S.Y. Cho, S.H. Kim, J. Xu, K.B. Kim, Ultrasoother, high electron mobility amorphous In-Zn-O films grown by atomic layer deposition, *Journal of Physical Chemistry C* 118 (2014) 408–415. <https://doi.org/10.1021/jp409738f>.
- [20] C.H. Ahn, H. Kim, H.K. Cho, Deposition of Al doped ZnO layers with various electrical types by atomic layer deposition, *Thin Solid Films* 519 (2010) 747–750. <https://doi.org/10.1016/J.TSF.2010.08.151>.
- [21] B. Macco, B.W.H. van de Loo, M. Dielen, D.G.J.A. Loeffen, B.B. van Pelt, N. Phung, J. Melskens, M.A. Verheijen, W.M.M. Kessels, Atomic-layer-deposited Al-doped zinc oxide as a passivating conductive contacting layer

- for n+-doped surfaces in silicon solar cells, *Solar Energy Materials and Solar Cells* 233 (2021) 111386. <https://doi.org/10.1016/J.SOLMAT.2021.111386>.
- [22] B. Macco, D. Deligiannis, S. Smit, R.A.C.M.M. Van Swaaij, M. Zeman, W.M.M. Kessels, Influence of transparent conductive oxides on passivation of a-Si:H/c-Si heterojunctions as studied by atomic layer deposited Al-doped ZnO, *Semicond Sci Technol* 29 (2014). <https://doi.org/10.1088/0268-1242/29/12/122001>.
- [23] N. Nosidlak, J. Jaglarz, P. Dulian, R. Pietruszka, B.S. Witkowski, M. Godlewski, W. Powroźnik, T. Stapiński, The thermo-optical and optical properties of thin ZnO and AZO films produced using the atomic layer deposition technology, *J Alloys Compd* 900 (2022) 163313. <https://doi.org/10.1016/J.JALLCOM.2021.163313>.
- [24] B. Macco, M.L. van de Poll, B.W.H. van de Loo, T.M.P. Broekema, S.B. Basuvalingam, C.A.A. van Helvoirt, W.J.H. Berghuis, R.J. Theeuwes, N. Phung, W.M.M. Kessels, Temporal and spatial atomic layer deposition of Al-doped zinc oxide as a passivating conductive contact for silicon solar cells, *Solar Energy Materials and Solar Cells* 245 (2022) 111869. <https://doi.org/10.1016/J.SOLMAT.2022.111869>.
- [25] R. Das, S. Ray, Transparent conducting zinc oxide as anti-reflection coating deposited by radio frequency magnetron sputtering, *Indian Journal of Physics* 86 (2012) 23–29. <https://doi.org/10.1007/s12648-012-0010-9>.
- [26] K.E. Lee, M. Wang, E.J. Kim, S.H. Hahn, Structural, electrical and optical properties of sol-gel AZO thin films, *Current Applied Physics* 9 (2009) 683–687. <https://doi.org/10.1016/J.CAP.2008.06.006>.
- [27] R. Singh, S.K. Mukherjee, RF sputtered AZO thin films: A potential TCO for various opto-electronic applications, *Mater Today Proc* (2023). <https://doi.org/10.1016/J.MATPR.2023.02.242>.

- [28] S.Y. Kuo, W.C. Chen, F.I. Lai, C.P. Cheng, H.C. Kuo, S.C. Wang, W.F. Hsieh, Effects of doping concentration and annealing temperature on properties of highly-oriented Al-doped ZnO films, *J Cryst Growth* 287 (2006) 78–84. <https://doi.org/10.1016/J.JCRYSGRO.2005.10.047>.
- [29] H. Cai, Z. Zhong, Q. Nong, P. Gao, J. He, Design and Optimization of SiO<sub>x</sub>/AZO Transparent Passivating Contacts for High-Efficiency Crystalline Silicon Solar Cells, *Adv Funct Mater* 34 (2024). <https://doi.org/10.1002/ADFM.202411207>.
- [30] E. Burstein, Anomalous Optical Absorption Limit in InSb, *Physical Reviews* (1954).
- [31] Y. Wu, A.D. Giddings, M.A. Verheijen, B. Macco, T.J. Prosa, D.J. Larson, F. Roozeboom, W.M.M. Kessels, Dopant Distribution in Atomic Layer Deposited ZnO:Al Films Visualized by Transmission Electron Microscopy and Atom Probe Tomography, *Chemistry of Materials* 30 (2018) 1209–1217. <https://doi.org/10.1021/acs.chemmater.7b03501>.
- [32] C. Seron, T. Desrues, F. Jay, A. Lanterne, F. Torregrosa, G. Borvon, Q. Rafhay, A. Kaminski, S. Dubois, Hydrogenation of sputtered ZnO:Al layers for double side poly-Si/SiO<sub>x</sub> solar cells, (n.d.). <https://doi.org/10.1051/epjpv/2022005>.
- [33] H. Werner, J. Lim, G. Zyna Kulesza-Matlak, M. Szindler, M.M. Szindler, M. Kiliszkiwicz, U. Wawrzaszek, A. Sypié, Ł. Major, K. Drabczyk, Innovative Deposition of AZO as Recombination Layer on Silicon Nanowire Scaffold for Potential Application in Silicon/Perovskite Tandem Solar Cell, *Energies* 2025, Vol. 18, Page 4193 18 (2025) 4193. <https://doi.org/10.3390/EN18154193>.
- [34] G. Shao. Work Function and Electron Affinity of Semiconductors: Doping Effect and Complication due to Fermi Level Pinning, *Energy &*

Environmental Materials 4 (2021) 273–276.

<https://doi.org/10.1002/EEM2.12218>.

- [35] Y. Wang, T.D.C. Hobson, J.E.N. Swallow, S. McNab, J. O’Sullivan, A.H. Soeriyadi, X. Niu, R.C. Fraser, A. Dasgupta, S. Maitra, P.P. Altermatt, R.S. Weatherup, M. Wright, R.S. Bonilla, Impact of precursor dosing on the surface passivation of AZO/AlO<sub>x</sub> stacks formed using atomic layer deposition, *Energy Advances* 4 (2025) 553–564.  
<https://doi.org/10.1039/D4YA00552J>.
- [36] J. Yun, J. Kim, H.S. Kojori, S.J. Kim, C. Tong, W.A. Anderson, Current enhancement of aluminum doped ZnO/n-Si isotype heterojunction solar cells by embedding silver nanoparticles, *J Nanosci Nanotechnol* 13 (2013) 5547–5551. <https://doi.org/10.1166/JNN.2013.7489>.
- [37] J. Panigrahi, Vandana, R. Singh, C.M.S. Rauthan, P.K. Singh, Crystalline silicon surface passivation by thermal ALD deposited Al doped ZnO thin films, *AIP Adv* 7 (2017). <https://doi.org/10.1063/1.4979326/1023166>.
- [38] K. Gao, D. Xu, J. Wang, Q. Bi, Z. Wu, H. Lin, S. Wang, W. Shi, C. Yu, F. Cao, Y. Diao, J. Xie, X. Wang, K. Li, X. Lou, W. Li, C. Xing, Y. Wang, T. Yan, D. Zhang, S. de Wolf, X. Zhang, X. Yang, Efficient Silicon Solar Cells with Aluminum-Doped Zinc Oxide-Based Passivating Contact, *Adv Funct Mater* (2024) 2415039. <https://doi.org/10.1002/ADFM.202415039>.
- [39] J. Meyer, S. Hamwi, M. Kröger, W. Kowalsky, T. Riedl, A. Kahn, Transition Metal Oxides for Organic Electronics: Energetics, Device Physics and Applications, *Advanced Materials* 24 (2012) 5408–5427.  
<https://doi.org/10.1002/ADMA.201201630>.
- [40] C. Battaglia, S.M. De Nicolás, S. De Wolf, X. Yin, M. Zheng, C. Ballif, A. Javey, Silicon heterojunction solar cell with passivated hole selective MoO<sub>x</sub> contact, *Appl Phys Lett* 104 (2014).  
<https://doi.org/10.1063/1.4868880/25311>.

- [41] J. Bullock, A. Cuevas, T. Allen, C. Battaglia, Molybdenum oxide MoO<sub>x</sub>: A versatile hole contact for silicon solar cells, *Appl Phys Lett* 105 (2014). <https://doi.org/10.1063/1.4903467/28810>.
- [42] H. Nasser, M.Z. Borra, E.H. Çiftçinar, B. Eldeeb, R. Turan, Fourteen percent efficiency ultrathin silicon solar cells with improved infrared light management enabled by hole-selective transition metal oxide full-area rear passivating contacts, *Progress in Photovoltaics: Research and Applications* 30 (2022) 823–834. <https://doi.org/10.1002/pip.3510>.
- [43] L.G. Gerling, S. Mahato, A. Morales-Vilches, G. Masmitja, P. Ortega, C. Voz, R. Alcubilla, J. Puigdollers, Transition metal oxides as hole-selective contacts in silicon heterojunctions solar cells, *Solar Energy Materials and Solar Cells* 145 (2016) 109–115. <https://doi.org/10.1016/J.SOLMAT.2015.08.028>.
- [44] Z. Wang, P. Li, Z. Liu, J. Fan, X. Qian, J. He, S. Peng, D. He, M. Li, P. Gao, Hole selective materials and device structures of heterojunction solar cells: Recent assessment and future trends, *APL Mater* 7 (2019) 110701. <https://doi.org/10.1063/1.5121327/122316>.
- [45] X. Liu, Q. Huang, X. Yang, J. Zhou, C. Ren, X. Su, Z. Xu, Y. Zhao, G. Hou, Simulation of p-type c-Si solar cells with metal oxides as carrier-selective contacts, *Solar Energy* 240 (2022) 84–89. <https://doi.org/10.1016/J.SOLENER.2022.05.030>.
- [46] Y. Jiang, S. Cao, L. Lu, G. Du, Y. Lin, J. Wang, L. Yang, W. Zhu, D. Li, Post-annealing Effect on Optical and Electronic Properties of Thermally Evaporated MoOX Thin Films as Hole-Selective Contacts for p-Si Solar Cells, *Nanoscale Res Lett* 16 (2021) 1–11. <https://doi.org/10.1186/s11671-021-03544-9>.
- [47] H. Mehmood, H. Nasser, T. Tauqeer, S. Hussain, E. Ozkol, R. Turan, Simulation of an efficient silicon heterostructure solar cell concept featuring

- molybdenum oxide carrier-selective contact, *Int J Energy Res* 42 (2018) 1563–1579. <https://doi.org/10.1002/ER.3947>.
- [48] R. García-Hernansanz, E. García-Hemme, D. Montero, J. Olea, A. Del Prado, I. Mártil, C. Voz, L.G. Gerling, J. Puigdollers, R. Alcubilla, Transport mechanisms in silicon heterojunction solar cells with molybdenum oxide as a hole transport layer, *Solar Energy Materials and Solar Cells* 185 (2018) 61–65. <https://doi.org/10.1016/j.solmat.2018.05.019>.
- [49] H. Nasser, F. Es, M. Zolfaghari Borra, E. Semiz, G. Kökbudak, E. Orhan, R. Turan, On the application of hole-selective MoOx as full-area rear contact for industrial scale p-type c-Si solar cells, *Progress in Photovoltaics: Research and Applications* 29 (2021) 281–293. <https://doi.org/10.1002/PIP.3363>.
- [50] L.G. Gerling, S. Mahato, C. Voz, R. Alcubilla, J. Puigdollers, Characterization of Transition Metal Oxide/Silicon Heterojunctions for Solar Cell Applications, *Applied Sciences* 2015, Vol. 5, Pages 695-705 5 (2015) 695–705. <https://doi.org/10.3390/APP5040695>.
- [51] J. Tong, T.T. Le, W. Liang, M.A. Hossain, K.R. McIntosh, P. Narangari, S. Armand, T.C. Kho, K.T. Khoo, Y. Zakaria, A.A. Abdallah, S. Surve, M. Ernst, B. Hoex, K.C. Fong, Impact of Pregrown SiOx on the Carrier Selectivity and Thermal Stability of Molybdenum-Oxide-Passivated Contact for Si Solar Cells, *ACS Appl Mater Interfaces* 13 (2021) 36426–36435. <https://doi.org/10.1021/acsami.1c06765>.
- [52] L. Cao, P. Procel, A. Alcañiz, J. Yan, F. Tichelaar, E. Özkol, Y. Zhao, C. Han, G. Yang, Z. Yao, M. Zeman, R. Santbergen, L. Mazzarella, O. Isabella, Achieving 23.83% conversion efficiency in silicon heterojunction solar cell with ultra-thin MoOx hole collector layer via tailoring (i)a-Si:H/MoOx interface, *Progress in Photovoltaics: Research and Applications* 31 (2023) 1245–1254. <https://doi.org/10.1002/PIP.3638>.

- [53] J. Bullock, M. Hettick, J. Geissbühler, A.J. Ong, T. Allen, C.M. Sutter-Fella, T. Chen, H. Ota, E.W. Schaler, S. De Wolf, C. Ballif, A. Cuevas, A. Javey, Efficient silicon solar cells with dopant-free asymmetric heterocontacts, *Nature Energy* 2016 1:3 1 (2016) 1–7.  
<https://doi.org/10.1038/nenergy.2015.31>.
- [54] J. Bullock, C. Samundsett, A. Cuevas, D. Yan, Y. Wan, T. Allen, Proof-of-concept p-type silicon solar cells with molybdenum oxide partial rear contacts, 2015 IEEE 42nd Photovoltaic Specialist Conference, PVSC 2015 (2015). <https://doi.org/10.1109/PVSC.2015.7356165>.
- [55] H.G. Tompkins, J.N. Hilfiker, *Spectroscopic Ellipsometry: Practical Application to Thin Film Characterization*, 1st ed., Momentum Press, LLC, New York, 2016.
- [56] H. Nasser, G. Altner, F. Çambay Kuban, E. Muka, R. Turan, Industrial PERC Solar Cells with Fully Passivated Rear Contact Enabled by Local Hole-Selective MoOx/Ag, *ACS Appl Energy Mater* 8 (2025) 7912–7918.  
<https://doi.org/10.1021/acsaem.4c03001>.
- [57] R.H. Cox, H. Strack, Ohmic contacts for GaAs devices, *Solid State Electron* 10 (1967) 1213–1218. [https://doi.org/10.1016/0038-1101\(67\)90063-9](https://doi.org/10.1016/0038-1101(67)90063-9).
- [58] N. Folchert, R. Brendel, Extended Cox & Strack analysis for the contact resistance of planar samples with carrier-selective junctions on both sides, *Solar Energy Materials and Solar Cells* 231 (2021) 111304.  
<https://doi.org/10.1016/J.SOLMAT.2021.111304>.
- [59] M. Van Rijnbach, R.J.E. Huetting, M. Stodolny, G. Janssen, J. Melskens, J. Schmitz, On the Accuracy of the Cox-Strack Equation and Method for Contact Resistivity Determination, *IEEE Trans Electron Devices* 67 (2020) 1757–1763. <https://doi.org/10.1109/TED.2020.2974194>.
- [60] H.C.M. Knoops, S.E. Potts, A.A. Bol, W.M.M. Kessels, Atomic Layer Deposition, *Handbook of Crystal Growth: Thin Films and Epitaxy: Second*

Edition 3 (2015) 1101–1134. <https://doi.org/10.1016/B978-0-444-63304-0.00027-5>.

- [61] Y. Wu, S.E. Potts, P.M. Hermkens, H.C.M. Knoops, F. Roozeboom, W.M.M. Kessels, Enhanced doping efficiency of Al-doped ZnO by atomic layer deposition using dimethylaluminum isopropoxide as an alternative aluminum precursor, *Chemistry of Materials* 25 (2013) 4619–4622. <https://doi.org/10.1021/cm402974j>.
- [62] S. Zogbo, W. Favre, M.E. Gueunier-Farret, O. Bonino, Method of contact resistivity measurements at typical operating conditions for silicon heterojunction solar cells, *Solar Energy Materials and Solar Cells* 286 (2025) 113584. <https://doi.org/10.1016/J.SOLMAT.2025.113584>.
- [63] C. Blaga, G. Christmann, M. Boccard, C. Ballif, S. Nicolay, B.A. Kamino, Palliating the efficiency loss due to shunting in perovskite/silicon tandem solar cells through modifying the resistive properties of the recombination junction †, (2021). <https://doi.org/10.1039/d1se00030f>.
- [64] T.G. Allen, J. Bullock, X. Yang, A. Javey, S. De Wolf, Passivating contacts for crystalline silicon solar cells, *Nature Energy* 2019 4:11 4 (2019) 914–928. <https://doi.org/10.1038/s41560-019-0463-6>.
- [65] C. Mader, J. Müller, S. Eidelloth, R. Brendel, Local rear contacts to silicon solar cells by in-line high-rate evaporation of aluminum, *Solar Energy Materials and Solar Cells* 107 (2012) 272–282. <https://doi.org/10.1016/J.SOLMAT.2012.06.047>.